Coumarin 6 Appended Phenanthroline-Based Cyclometalated Ir(III) Photocatalysts for NADH Oxidation and ROS-Mediated Anticancer Activity Under Normoxic and Hypoxic Conditions

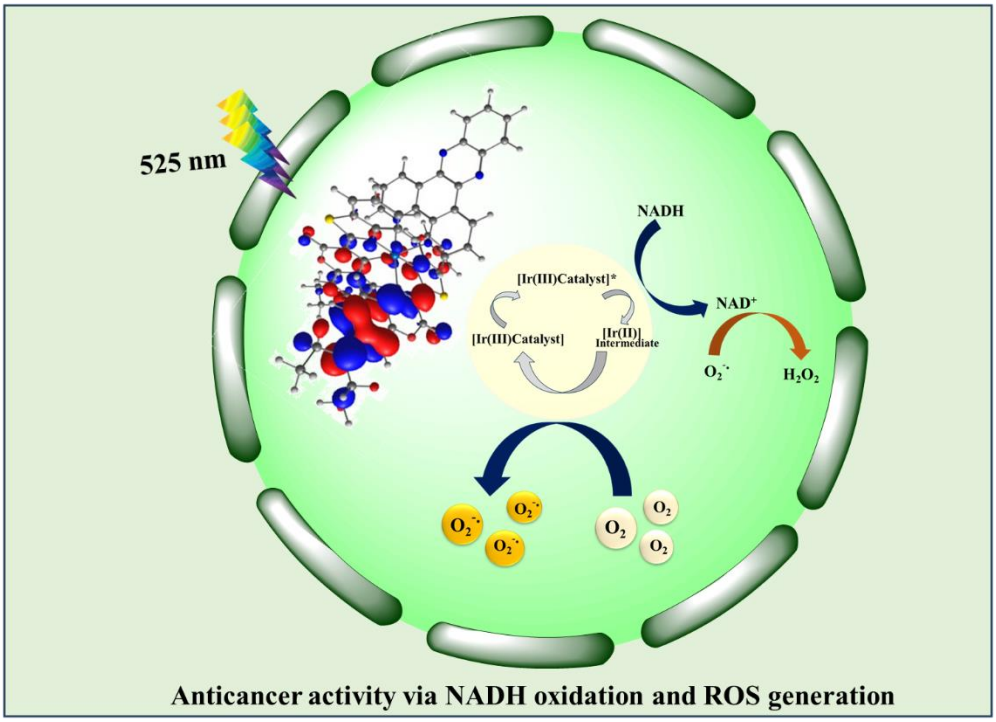

Published in *Inorg. Chem. Front*. **2024**, *11*, 5435-5448. **(Highlighted as Journal Front Cover)**

3.1. Abstract

Herein, we have designed, synthesized, and characterized three novel coumarin 6-based Ir(III) photocatalysts *viz.*, $[Ir(CO6)_2(phen)]Cl$ **(4)**, $[Ir(CO6)_2(dppz)]Cl$ **(5)**, and $[Ir(CO6)_2(aip)]Cl$ **(6)**, where, CO6 = coumarin 6, phen = 1,10-phenanthroline, dppz = dipyrido[3,2-a:2',3'-c]phenazine, and aip = 2-(anthracen-9-yl)-1H-imidazo[4,5-f][1,10]phenanthroline. Coumarin 6 introduced a green light absorption property. When exposed to green light, **4**-**6** demonstrated catalytic NADH photo-oxidation with TOF *ca.* 840-1000 h^{-1} in PBS, comparable or higher to the highest achieved TOF with previously reported Ir(III)-based photo-catalysts for NADH oxidation. **4**-**6** also generated $^1O_2$ on green light irradiation. These photocatalysts showed photo-toxicities against human lung adenocarcinoma cells (A549) and human cervical cancer cell line (HeLa) cells with the IC_{50} and PIs (Dark IC_{50}/Light IC_{50}) in the range of 0.5-1.6 μM and > 28-71, respectively. Interestingly, these photocatalysts did not show any notable toxicities toward the normal human bronchial epithelial (BEAS-2B) cell line in the dark. The selectivity index (SI = Light IC_{50} in normal cells/Light IC_{50} in cancer cells) of **4**-**6** for cancer cell killing was in the range of 7-19. Moreover, photocatalysts **5** and **6** also showed good phototoxicity against A549 cancerous cells under hypoxic conditions, revealing their potential for hypoxic tumor treatment. The mechanistic investigation of the most potent photocatalyst **6** in A549 cells revealed that it localized in the mitochondria, generated ROS, and oxidized NADH during light exposure, ultimately causing cell apoptosis via mitochondrial depolarization. This strategy of killing cancer cells by combining type-I and type-II mechanisms, *i.e.*, via NADH

oxidation, H_2O_2, $^{\bullet}OH$, and $^1O_2$ generation, could provide efficient photo-activated chemotherapy.

3.2. Introduction

We have described three cyclometallated Ir(III) photocatalysts in **Chapter II**, *viz*., $[Ir(C^N)_2(ip)]Cl$ (**1**), $[Ir(C^N)_2(ph\text{-}ip)]Cl$ (**2**) and $[Ir(C^N)_2(aip)]Cl$ (**3**) (C^N = 2-(4-(Trifluromethyal)phenyl)pyridine; ip = 1H-imidazo[4,5-f][1,10]phenanthroline; ph-ip = 2-phenyl-1H-imidazo[4,5-f][1,10]phenanthroline; aip = 2-(anthracene-9-yl)-1H-imidazo[4,5-f][1,10]phenanthroline). These photocatalysts exhibited excellent photoinduced NADH oxidation turnover frequencies (TOFs), surpassing most of the previously reported Ir(III)-based photocatalysts. Furthermore, these photocatalysts demonstrated significant cytotoxicity against cancer cells under visible light irradiation. However, despite these promising results, their absorption remained confined to the blue light region, which is not ideal for biological applications due to low tissue penetration power.[1] To overcome this limitation and to enhance the photocatalytic performance, we designed a new series of coumarin 6-containing cyclometallated Ir(III) photocatalysts by incorporating 1,10-phenanthroline and its derivatives as polypyridyl ligands. This strategy successfully red-shifted the absorption into the green light region and simultaneously achieved very high TOFs.

The selection of coumarin 6 was motivated by its well-known ability to shift absorption toward the green-light region and its intrinsic fluorescent properties, which facilitated in-cell

tracking and localization studies.[2-4] Additionally, Ir(III)-coumarin conjugates have been previously explored for diverse applications, including oxygen sensing, singlet oxygen generation, anticancer and antibacterial therapies, antioxidant activities, fluorescent probe sensing, and microRNA detection.[5,6]

Furthermore, 1,10-phenanthroline and its derivatives were chosen due to their strong light-absorbing properties, supporting visible light-induced photocytotoxicity.[7,8] The extended π-conjugation in dppz and aip ligands was anticipated to decrease the HOMO-LUMO energy gap and enhance the photocatalysts' electron-accepting ability and reduction potential, thereby improving their photocatalytic efficacy.[9,10]

Herein, we performed the synthesis, characterization, green light-induced in-solution ROS generation, and NADH oxidation, visible light-induced cytotoxicity, and intracellular change in concentration ratio of NAD^+/NADH property of three cyclometallated Ir(III) based photocatalysts *viz.*, $[Ir(CO6)_2(phen)]Cl$ **(4)**, $[Ir(CO6)_2(dppz)]Cl$ **(5)**, and $[Ir(CO6)_2(aip)]Cl$ **(6)**, (**Figure 3.1**).[2] Photocatalyst **4** has been structurally characterized by X-ray crystallography. Significant results of this work include (i) NADH photo-oxidation by the photocatalysts with very high TOF in an aqueous solution upon green light exposure, (ii) Visible light-triggered anticancer activities of **4-6** at sub-micromolar concentration with notably high photo-cytotoxicity index (PI) and selectivity index (SI), (iii) The ability of photocatalyst **6** to photo-oxidize NADH within cells, (iv) Mitochondrial localization of **6** and thereafter ROS generation and NADH oxidation on light exposure to induce cell apoptosis *via* mitochondrial depolarization by combining type-I and type-II mechanisms.

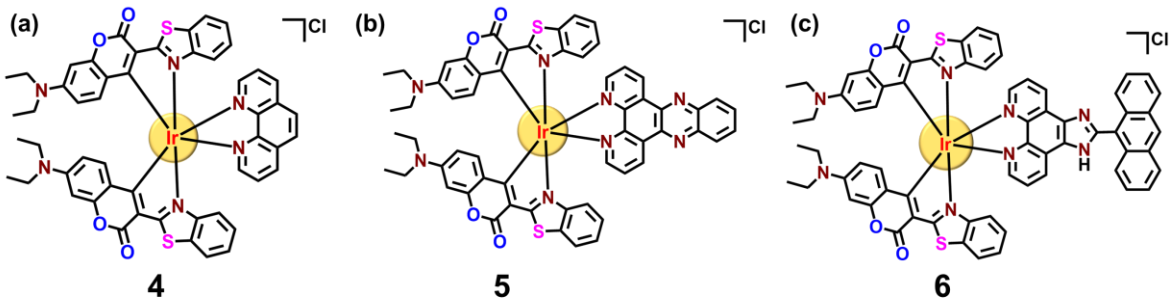

Figure 3.1: Structures of (a) **4**, (b) **5**, and (c) **6**.

3.3. Results and Discussion

3.3.1 Synthesis and Characterization

Synthesis of **4-6** involved the reaction of coumarin 6-coordinated Ir(III) μ-chloro-bridged dimers with different bidentate ligands in $CHCl_3$ and MeOH (in a ratio of 3:1, v/v) under reflux conditions. The resulting photocatalysts were purified through recrystallization from methanol. The photocatalysts were characterized from various spectroscopic data such as HR-MS, ^1H and ^{13}C NMR, HPLC, ESI-MS, UV-Vis., and fluorescence data. The ESI-MS analysis of **4** showed a molecular ion peak at m/z = 1071.2358 corresponding to $[M]^+$ ion (Figure 3.2a). Similarly, HRMS spectra of **5** and **6** showed a molecular ion peak at m/z = 1173.2549 and 1287.2974, respectively, corresponding to molecular ion $[M]^+$ (Figures 3.2b, c). The ^1H and ^{13}C NMR spectra of photocatalysts **4-6** recorded in DMSO-d_6 (Figures 3.3a-f) reflected the structural compositions. The ^1H NMR spectra reveal well-resolved signals that support the proposed structure. The peaks observed in the aromatic region (δ ~5.5–10 ppm) correspond to the aromatic protons of the coumarin 6, phen, dppz, and aip ligands,

consistent with the expected integration and chemical shifts (Figures 3.3a-c).[3,4,11] A distinct triplet at δ = 0.97 ppm was assigned to the terminal methyl (–CH_3) protons of the ethyl group of -NCH_2CH_3 unit of coumarin 6, while a corresponding quartet around δ = 3.3 ppm confirmed the presence of the adjacent methylene (–CH_2–) protons.[3,4,11] Characteristic signals for aromatic carbons were observed in the range of δ = 110–180 ppm (Figures 3.3d-f). To further validate the purity of photocatalysts **4-6**, high-performance liquid chromatography (HPLC) analysis was performed. From the HPLC chromatograms (Figures 3.4a, b), the purity of **6** was determined to be ~99%, whereas **5** exhibited a purity of ~96%.

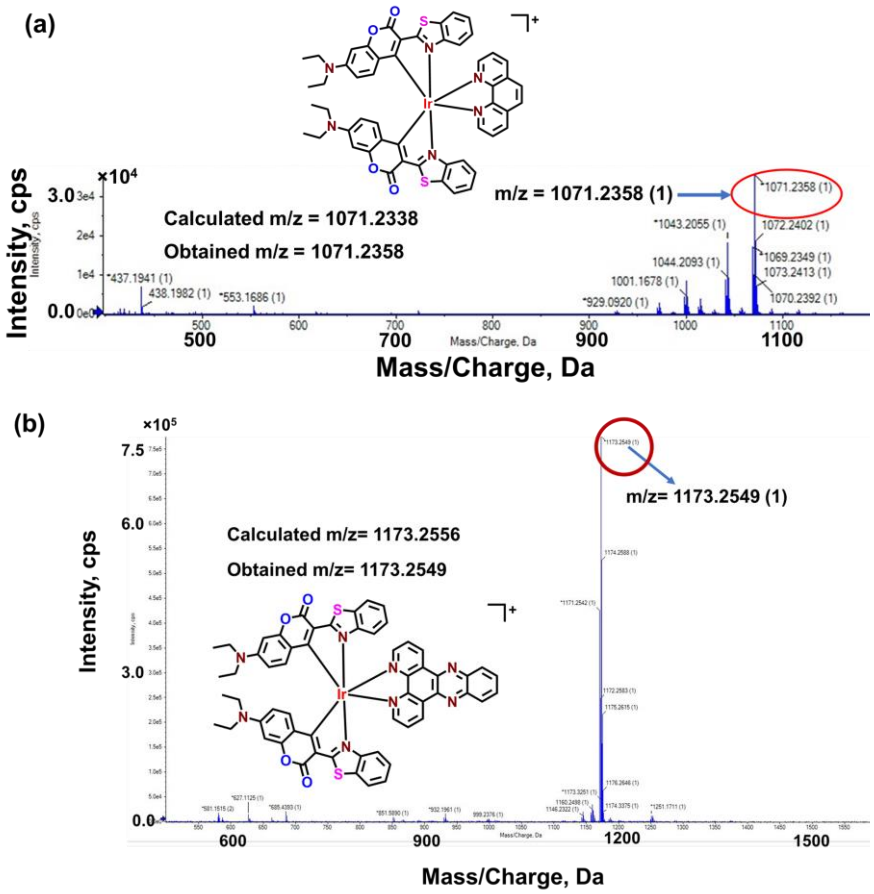

Figure 3.2: ESI-MS spectra of photocatalyst (a) **4** and HRMS spectra of (b) **5** in acetonitrile.

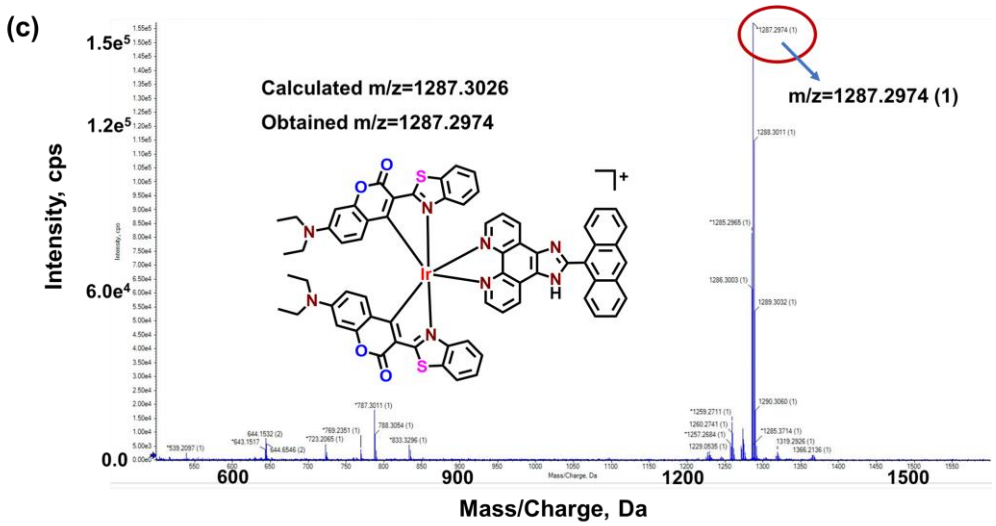

Figure 3.2: (c) HRMS spectra of **6** in acetonitrile.

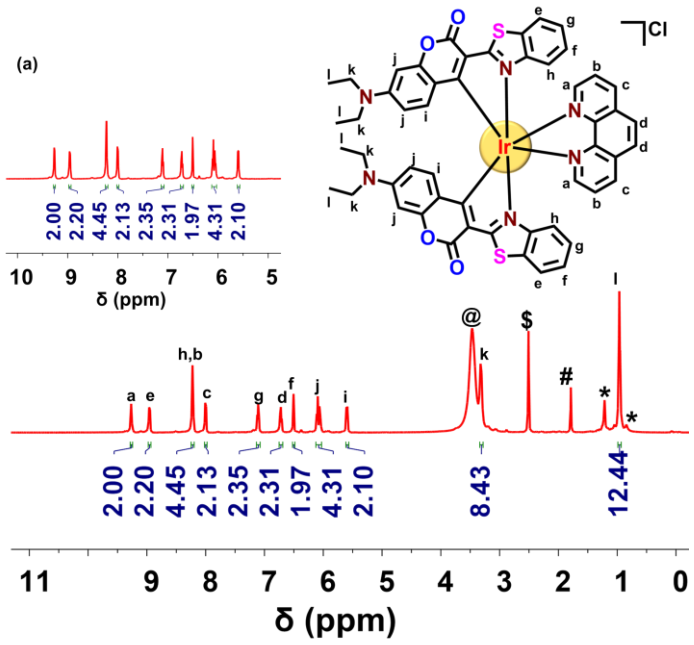

Figure 3.3: (a) ^{1}H NMR spectra of **4** in DMSO-d_6 (500 MHz). (Residual solvent peaks: $^{@}H_2O$, $^{\$}$DMSO-$d_6$, *n-hexane).

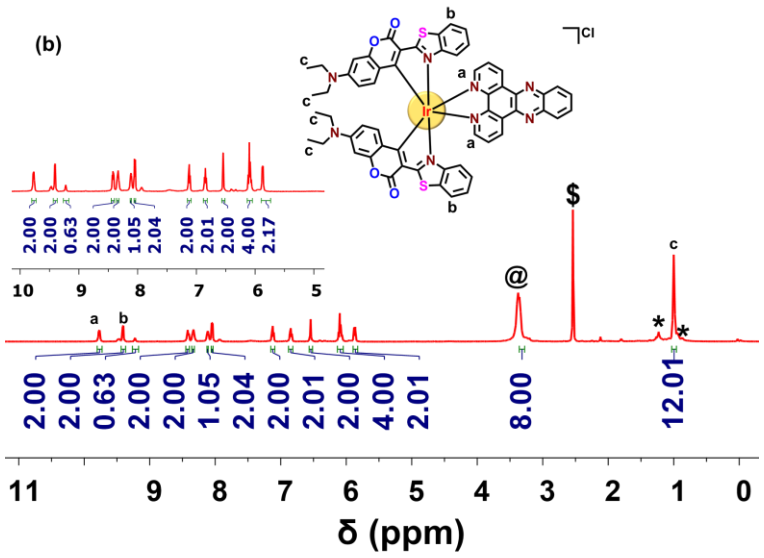

Figure 3.3: (b) ^{1}H NMR spectra of **5** in DMSO-d_6 (500 MHz). (Residual solvent peaks: $^{@}H_2O$, $^{\$}$DMSO-$d_6$, *n-hexane).

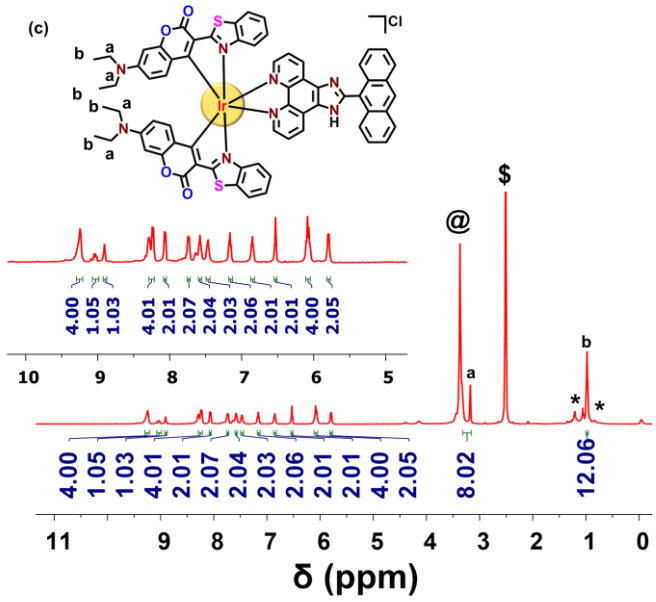

Figure 3.3: (c) ^{1}H NMR spectra of **6** in DMSO-d_6 (500 MHz). (Residual solvent peaks: $^{@}H_2O$, $^{\$}$DMSO-$d_6$, *n-hexane).

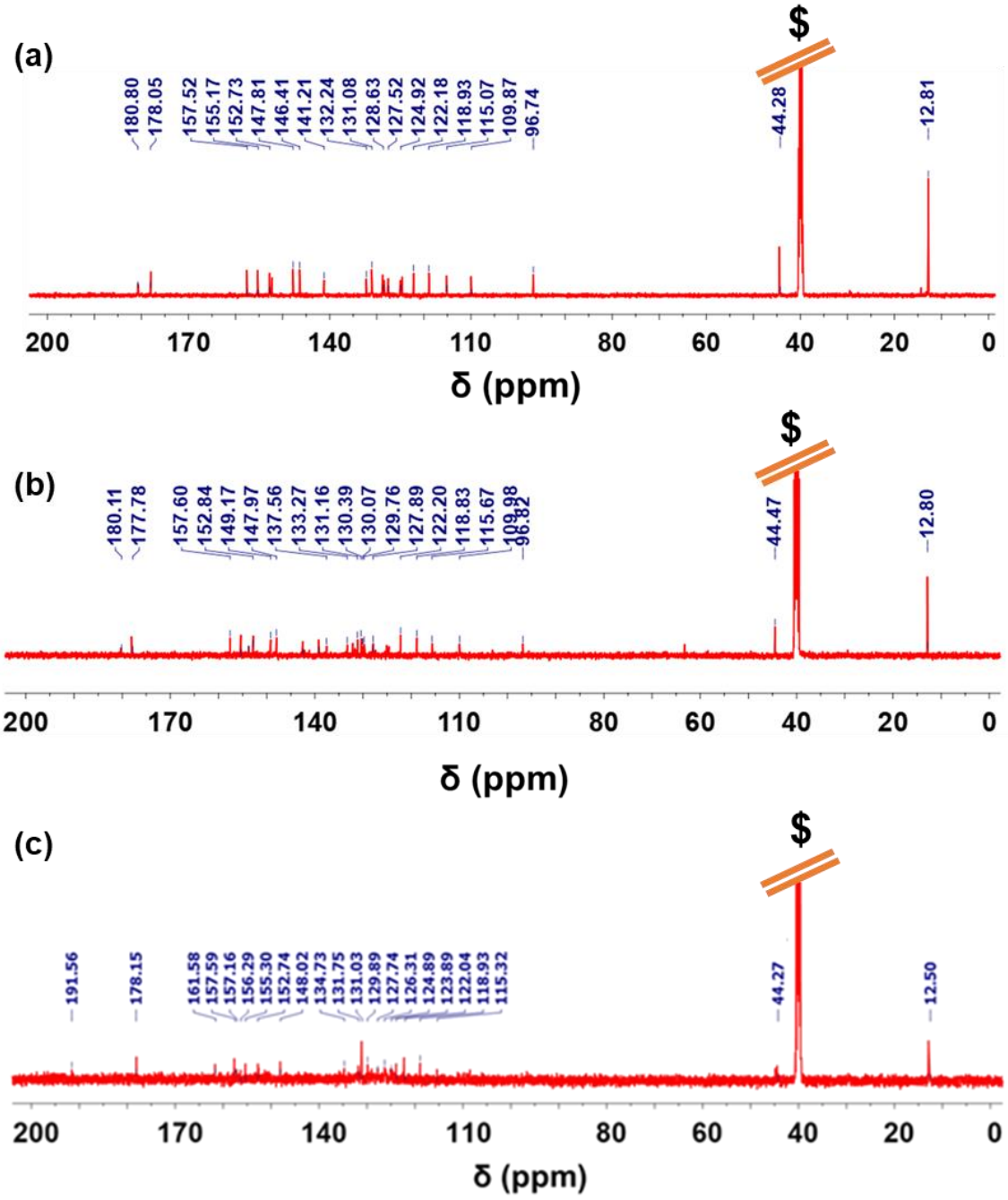

Figure 3.3: ^{13}C NMR spectra of (d) **4**, (e) **5**, and (f) **6** in DMSO-d_6 (125 MHz) (Residual solvent peaks: $^{\$}$DMSO-$d_6$). The residual solvent peak was cutted for clarity.

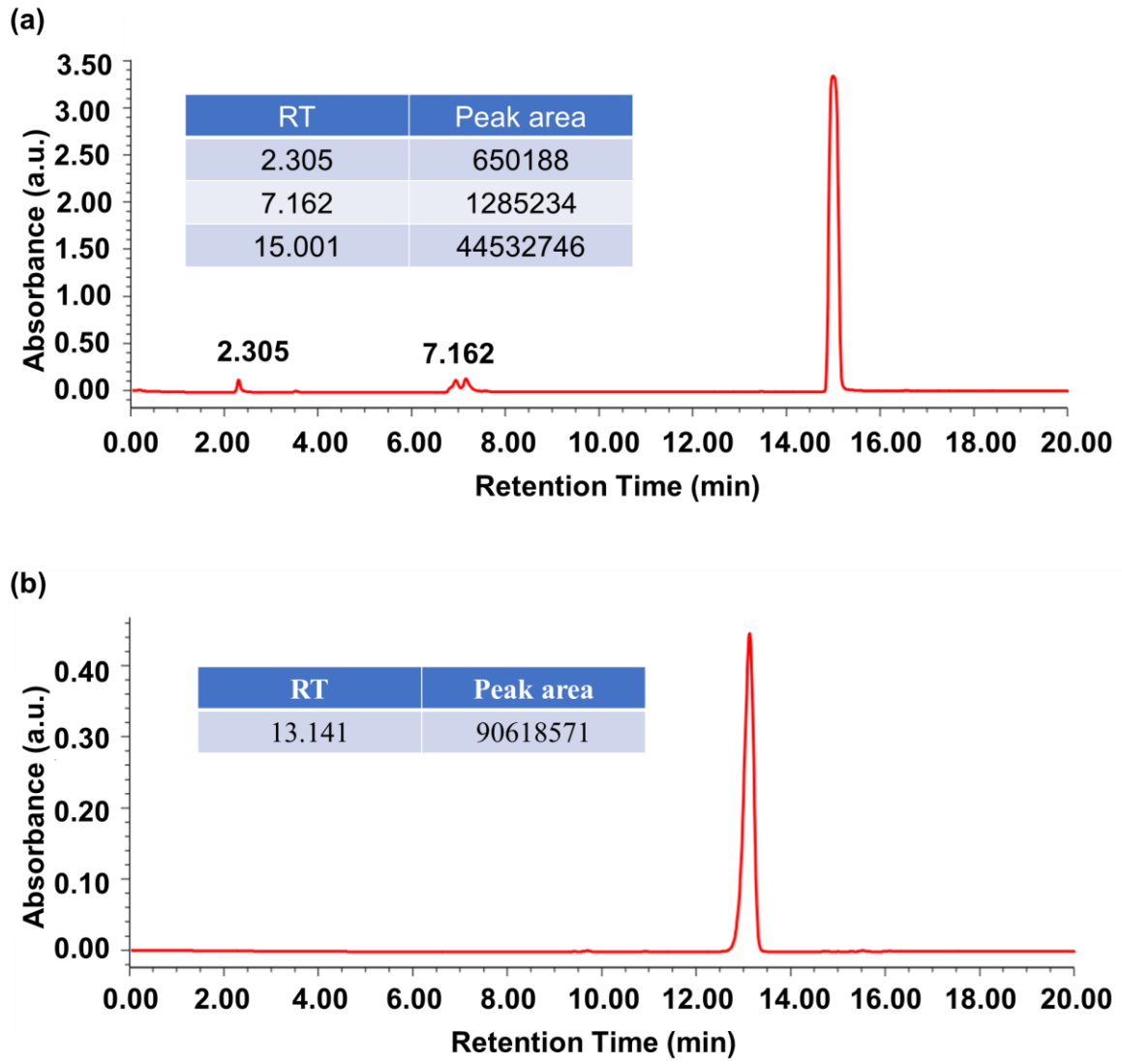

Figure 3.4: High-performance liquid chromatography (HPLC) data of photocatalysts (a) **5** and (b) **6** using HPLC column: Chromasol ONYX C18, (250 mm x 4.0 mm), 5 micron, 100Å; Mobile Phase: ACN/Water; Flow: 0.8 mL/min; Injection volume: 15 µL; Detector: UV (254 nm); Instrument: Waters 2489.

3.3.2. Electronic Spectra

The absorption spectra of photocatalysts **4-6** in DMSO showed a sharp band between 480-550 nm, corresponding to the intra-ligand π to π* transition in coumarin 6, and a broad band between 400-450 nm, corresponding to MLCT (Figure 3.5a).[3,4] These absorption bands in the green light region suggested that **4-6** can absorb green light, making them suitable candidates for photoinduced applications, including green light-triggered NADH oxidation.

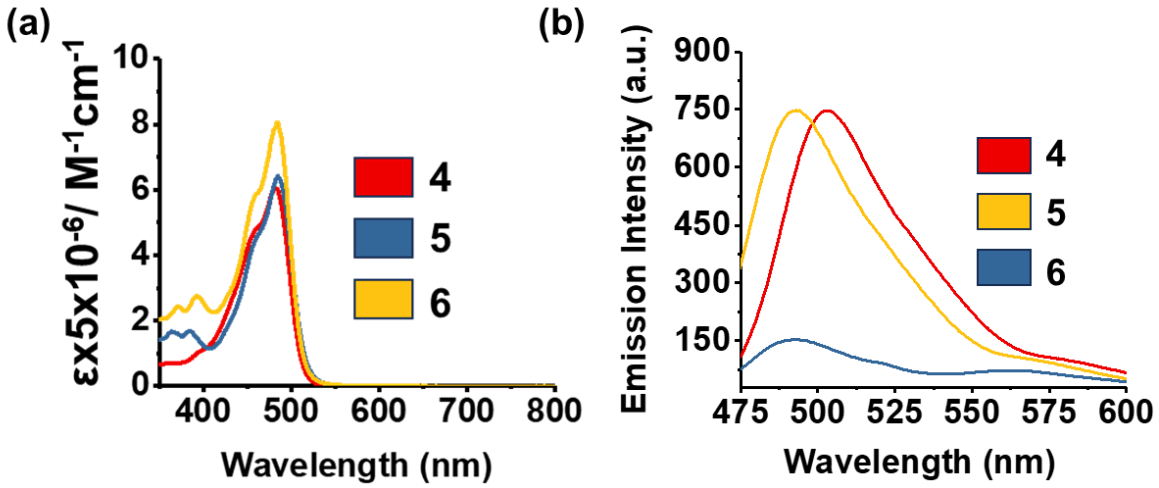

Figure 3.5: (a) Absorption spectra of photocatalysts **4-6** in DMSO; (b) Emission spectra of photocatalysts **4-6** (20 μM each) in DMSO:H_2O (1:9, v/v) [λ_{ex} = 460 nm].

The fluorescence properties of photocatalysts **4-6** were investigated in DMSO:H_2O (1:9, v/v) to evaluate their potential for cellular imaging. When excited at 460 nm, all the photocatalysts exhibited prominent green fluorescence emission (Figure 3.5b), characteristic of the coumarin 6 moiety incorporated as a ligand.[3,4] The observed emission strongly supported the retention of the coumarin fluorophore's photophysical properties after complexation with

Ir(III). The green emissive nature of **4-6** is particularly advantageous for cellular imaging, enabling real-time monitoring of their cellular uptake and subcellular localization.

3.3.3. Crystal Structure

Photocatalyst **4** was structurally characterized by single-crystal X-ray crystallography. The photocatalyst was crystallized in the $P\bar{1}$ space group of the triclinic crystal system. The ORTEP view and the unit cell packing diagram for the photocatalyst are shown in Figure 3.6 and Figure 3.7, respectively. The structure showed an Ir(III) centre bonded to the chelating N,N-donor 1,10-phenanthroline, and C, N-donor coumarin 6, giving an $Ir^{III}C_2N_4$ coordination in a distorted octahedral geometry. The Ir-N and Ir-C bond distances are in the range of 2.077 to 2.138 Å

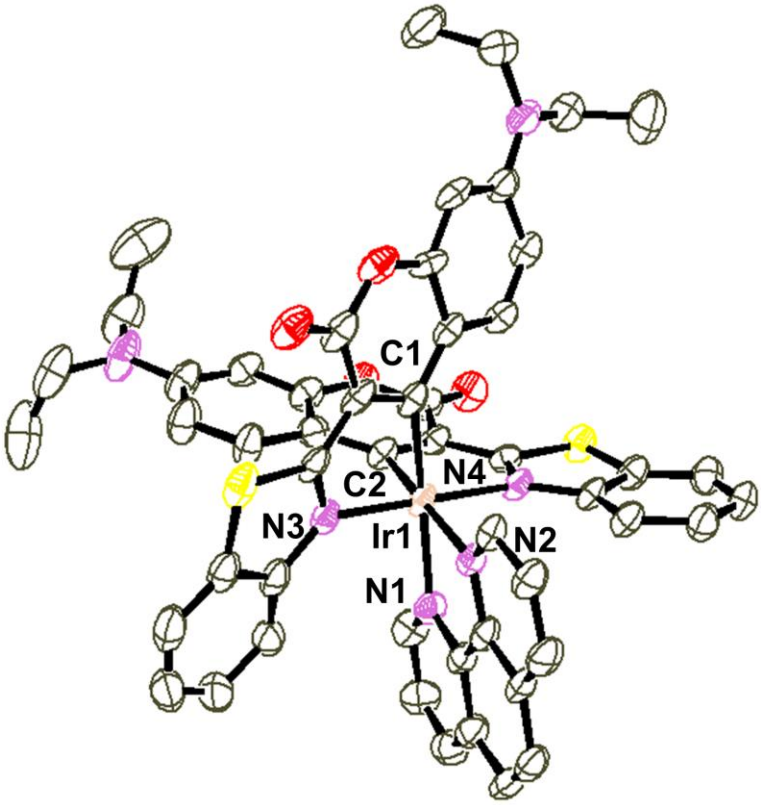

Figure 3.6: An ORTEP view of **4** with atom labeling scheme. The thermal ellipsoids are shown at a 50% probability level. The hydrogen atoms and counter ion are not shown for clarity.

and 2.030 to 2.036 Å, respectively (Table 3.1). The Ir1-N1 bond distance is 2.147 Å (Table 3.1). The Ir1-C1 bond distance trans to Ir1-N1 is 2.036 Å, which confirmed the distorted octahedral geometry around the Ir(III) centre. A similar distorted octahedral structure was also reported by Ruiz *et al*.[8] They have reported almost similar Ir-N and Ir-C bond distances of 2.131 Å and 2.015 Å, respectively.[8] The N3–Ir1–C1 angle is characteristically small (80.2°) compared to N3–Ir1–C1 angle (95.2°) reported by Ruiz *et al*.[8] In another study by Kokare *et al*. reported Ir-N and Ir-C bond distances of 2.145 (4) Å and 2.076 (5)Å, respectively.[7] Similarly, Khatua *et al*. also reported Ir-N and Ir-C bond distances of 2.162 Å and 2.008 Å, respectively.[10]

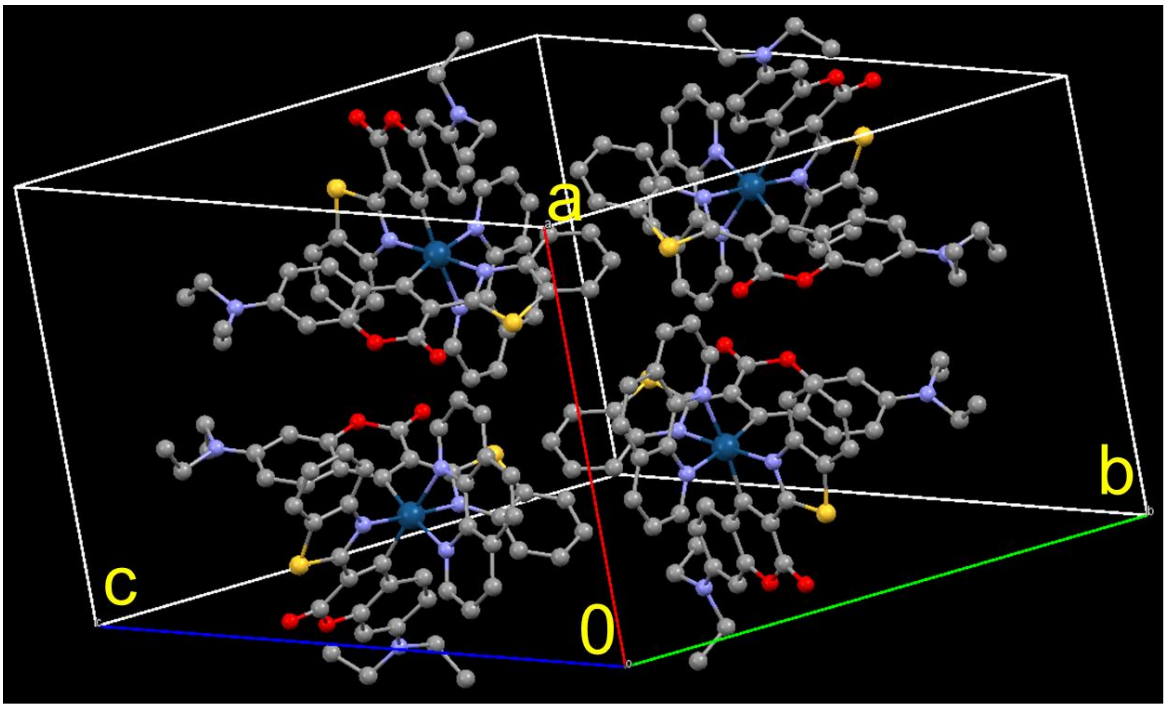

Figure 3.7: Unit cell packing diagram of $[Ir(CO6)_2(phen)]Cl$ **(4)**.

Table 3.1: Selected bond distances (Å) and bond angles (°) for $[Ir(CO6)_2(phen)]Cl$ **(4)** with e.s.d.s in the parentheses.

	Bond distances (Å)	Bond angles (°)	
Ir1-N3	2.077(4)	N3-Ir1-N1	96.1(2)
Ir1-N1	2.147(5)	N3-Ir1-N4	177.9(2)
Ir1-N4	2.071(4)	N3-Ir1-N2	83.8(2)
Ir1-N2	2.138(6)	N3-Ir1-C2	99.9(2)
Ir1-C2	2.030(5)	N3-Ir1-C1	80.2(2)
Ir1-C1	2.036(6)	C2-Ir1-C1	87.9(2)

3.3.4. Light Stability

To evaluate the stability of the photocatalysts, the UV–Vis. absorption spectra of **4-6** were monitored over time under visible light irradiation (400-700 nm, 10 J cm^{-2}) (Figures 3.8a-c). As shown in Figures 3.8a-c, all the photocatalysts exhibited minimal changes in their absorption profiles over extended periods of light irradiation, indicating excellent resistance to photodegradation. This suggested that the structural integrity of the photocatalysts remains intact under light exposure, a property critical for maintaining consistent photochemical performance during biological and catalytic applications.[3,4,12]

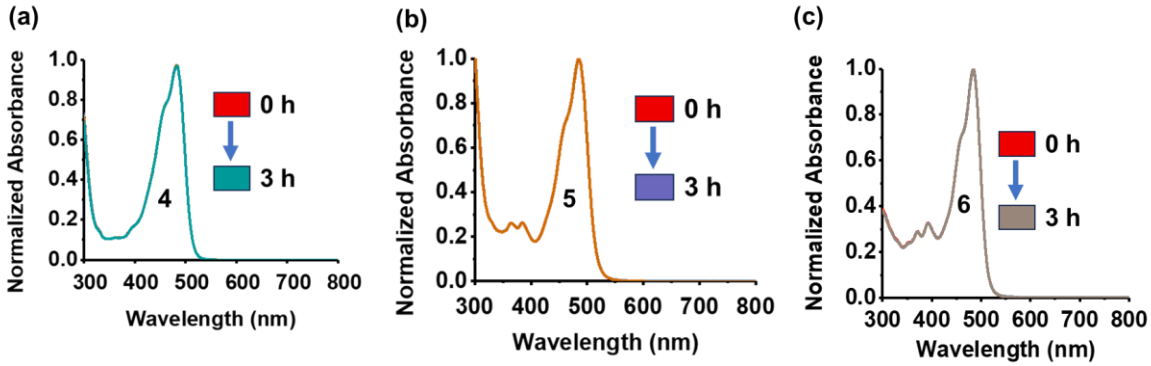

Figure 3.8: (a), (b), and (c) represent photo-stability of **4-6**, respectively, under exposure to white light (400-700 nm, 10 J cm^{-2}) at various time intervals in 0.5 % DMSO and 99.5 % PBS.

3.3.5. DFT Calculation

To obtain detailed insight into the electronic structure of **4-6**, the density functional theory (DFT) calculations were employed at the B3LYP/LANL2DZ level using Gaussian 16 software.[13] The ground state optimized structures of **4-6** revealed a distorted octahedral geometry around the Ir(III) center as reported in the literature.[12] The obtained FMOs from calculations, as shown in Figure 3.9, presented the specific features for **4-6**. In photocatalyst **4**, the HOMO was predominantly localized around Ir(III) center and coumarin 6 moieties, while the LUMO was mainly concentrated on the 1,10-phenanthroline moiety (Figure 3.9). For photocatalysts **5** and **6**, the HOMO was also primarily based on Ir(III) center and coumarin 6 moiety similar to **4**. However, the LUMO was centered on the dppz moiety in case of **5**, and in case of **6**, it was accumulated on the 1,10-phenanthroline moiety of the attached aip ligand (Figure 3.9). The energy gap between HOMO and LUMO in

photocatalysts **4-6** was significantly lower (ΔE_g < 2.3 eV), suggesting that these photocatalysts could be effective photosensitizers that can be activated with visible light.[12,14]

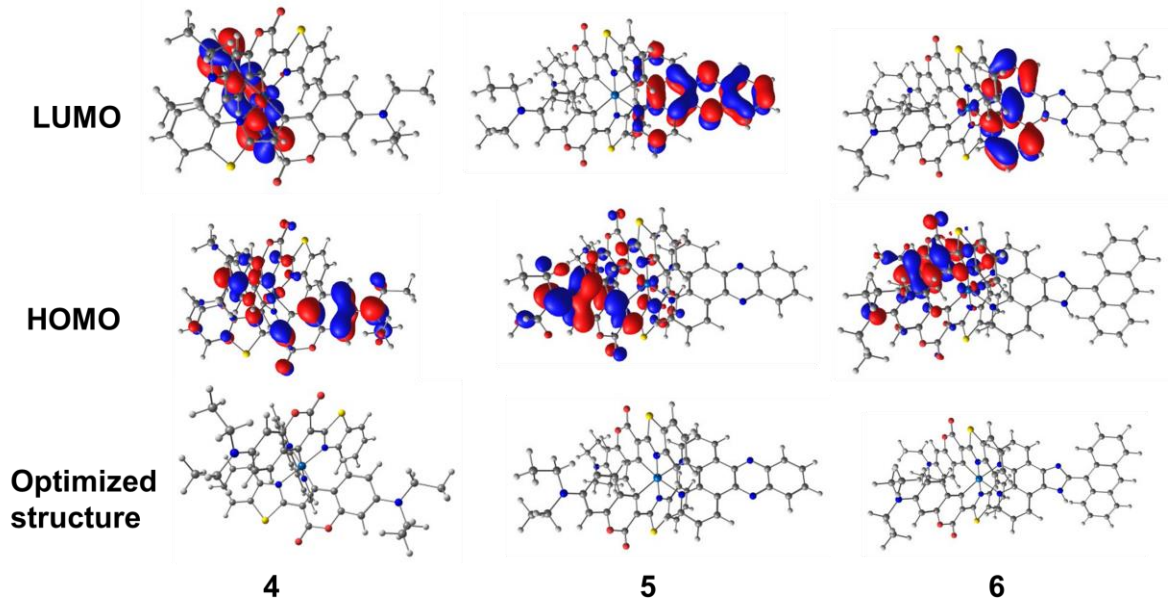

Figure 3.9: The energy-optimized structures, HOMO, and LUMO of photocatalysts **4-6**.

Any compound that aspires to act as a PS must have a first excited triplet state greater than 0.98 eV with respect to S_0, that is, the energy differential between the ground state and the first excited singlet state of $^3O_2$.[15] Further, the absorption maxima and ISC process form singlet to triplet excited states determine the efficacy of PS in the PDT process.[14,15] Therefore, TD-DFT calculation was carried out to gain insight into the excited state properties of **5** and **6** (Figure 3.10). The calculated ten lowest vertical singlet–singlet/triplet transition energies are given in Tables 3.2 and 3.3. The obtained result revealed that the

lowest-lying triplet state of **5** and **6** is of sufficient energy to generate singlet oxygen (Figure 3.10).

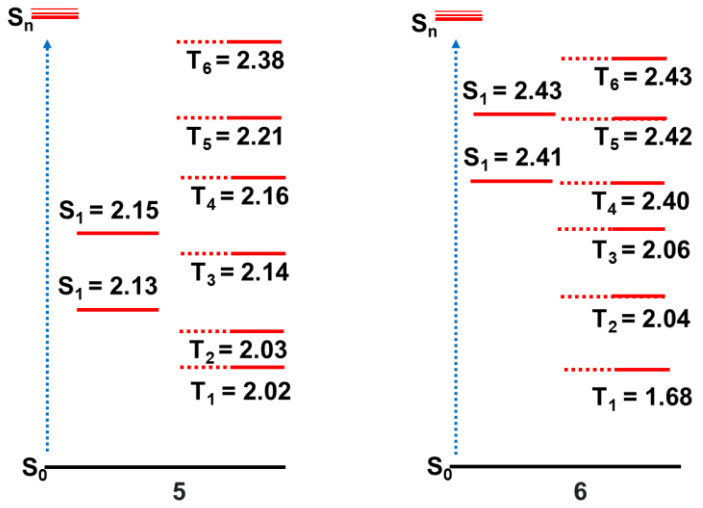

Figure 3.10: Vertical energy levels of the different electronic states of **5** and **6** obtained from TD-B3LYP/LANL2DZ/6-31g* in water. All energy values are in eV.

Table 3.2: Energy (eV) of the lowest vertical 10 singlet–singlet ($S_0 \rightarrow S_n$; n = 1 to 10) transitions for the photocatalysts computed at the TD-B3LYP/LANL2DZ/6-31g* level of theory in water. The oscillator strengths are indicated in parentheses.

Singlet state	**Energy (eV) of the lowest vertical 10 singlet–singlet transition**	
	5	**6**
S1	2.125 (0.0063)	2.408 (0.0181)

S2	2.147 (0.0047)	2.428 (0.0070)
S3	2.392 (0.0045)	2.513 (0.0651)
S4	2.411 (0.0016)	2.575 (0.1135)
S5	2.546 (0.1263)	2.588 (0.0738)
S6	2.559 (0.0748)	2.712 (0.6292)
S7	2.697 (0.4638)	2.734 (0.777)
S8	2.712 (0.4994)	2.745 (0.0086)
S9	2.844 (0.5072)	2.905 (0.3110)
S10	2.845 (0.050)	2.916 (0.0511)

Table 3.3: Energy (eV) of the lowest vertical 10 singlet–triplet ($S_0 \rightarrow T_n$; n = 1 to 10) transitions for the photocatalysts computed at the TD-B3LYP/LANL2DZ/6-31g* level of theory in water.

Triplet state	**Energy (eV) of the lowest vertical 10 singlet–triplet transition**	
	5	**6**

T_1	2.025	1.684
T_2	2.030	2.047
T_3	2.143	2.052
T_4	2.156	2.398
T_5	2.212	2.423
T_6	2.383	2.432
T_7	2.405	2.574
T_8	2.558	2.582
T_9	2.563	2.596
T_{10}	2.596	2.752

3.3.6. NADH Photo-oxidation

The photocatalytic NADH oxidation potential of **4-6** was explored using UV-Vis. spectroscopy by monitoring the time-dependent decrease in the NADH-based band at *ca.* 339 nm.[3,4,12,14, 16-18] Under irradiation with green light (525 nm, 50.2 J cm^{-2}), the photocatalysts caused a significant decrease in the absorbance of NADH (Figures 3.11a-c). The formation of NAD^+ due to the NADH photo-oxidation was evident from the increase in

the NAD^+-based peak at *ca.* 265 nm (Figures 3.11a-c). **6** exhibited the highest catalytic activity among **4-6**, achieving a TOF of 1003.5±24.6 h^{-1}, followed by **5** and **4**, which displayed TOF values of 841.4±45.8 h^{-1} and 621.4±90.6 h^{-1}, respectively (Table 3.4). These observed values are much higher than the previously reported Ir(III) photocatalysts, **Ir1** (33.6 h^{-1}), **Ir8** (126.4 h^{-1}), **Ir9** (735.1 h^{-1}), **Ir12** (270.6 h^{-1}), **Ir23** (16.9 h^{-1}), **Ir24** (42.8 h^{-1}), **Ir25** (414.2 h^{-1}).[7,12,14,17] Importantly, the TOF achieved in the case of **6** (TOF = 1003.5±24.6) is much higher than the TOF achieved by the highly active photocatalyst **3** (TOF = 697.4±26.4), as we reported in **Chapter II**. In aip ligand, the extended conjugation is more than that of dppz. So, the reduction potential might be higher in the case of **6**. This was also supported by the cyclic voltammetry data (Figure 3.11d). The higher reduction potential of **6** indicated its higher electron-accepting tendency than **5**, making **6** a better NADH oxidant. Overall, the above results revealed that photocatalysts **4-6** could be used as effective photo-catalysts for NADH oxidation and might alter the

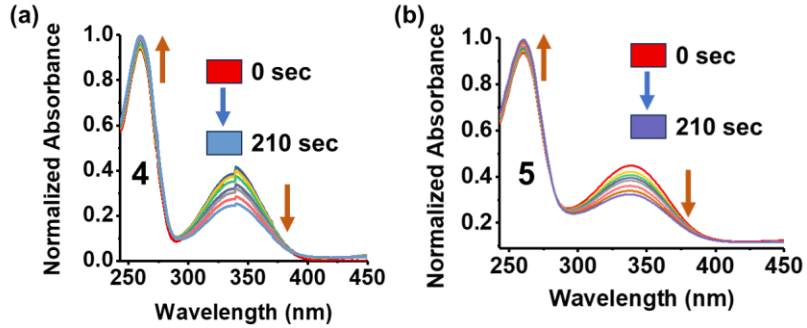

Figure 3.11: (a) and (b), Green light-induced NADH (240 μM) oxidation by photocatalysts **4** and **5** (2 μM each), respectively, monitored by UV-Vis. spectroscopy at different time intervals in 0.5% DMSO/99.5% PBS (v/v) solution (Light source: 525 nm, 50.2 J cm^{-2}). The experiment was repeated three times independently.

mitochondrial ETC, resulting in mitochondrial depolarization and cell death.[3,4,8,12,14,16-18] Interestingly, during the photocatalytic NADH oxidation, the generation of hydrogen peroxide (H_2O_2) was detected using peroxide detection strips (Figure 3.12a). Notably, no significant H_2O_2 production was observed in the dark (Figure 3.12a). However, as the light exposure time was increased, the color intensity of the H_2O_2 strip increased, indicating more and more H_2O_2 generation (Figure 3.12b). This was due to the increased consumption of NADH (Figure 3.12c). This indicated that H_2O_2 was a byproduct of the NADH photocatalytic oxidation by the photocatalysts via a type I pathway.[3,4,12,14] As reported by Sadler and coworkers for the

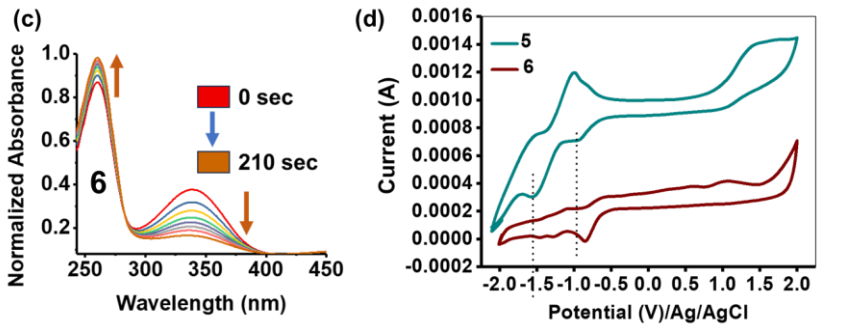

Figure 3.11: (c) Green light-induced NADH (240 μM) oxidation by photocatalysts **6** (2 μM), monitored by UV-Vis. spectroscopy at different time intervals in 0.5% DMSO/99.5% PBS (v/v) solution (Light source: 525 nm, 50.2 J cm^{-2}). The experiment was repeated three times independently. The outcome of the results was expressed as mean ± SD. (d) The CV profiles of the **5** and **6** (1.0 mM each) in acetonitrile containing tetrabutylammonium hexafluorophosphate (0.1 M) as a supporting electrolyte using a three-electrode system with with a glassy carbon electrode as the working electrode, saturated calomel electrode as the reference electrode, and platinum wire as the counter electrode.

Ir(III) photocatalyst, the photocatalytic mechanism here might involve the steps like (i) Ir(III) catalyst at the triplet excited state accepts an electron from NADH, and resulting Ir(II) intermediate and $NADH^{\bullet+}$ (ii) Regeneration of Ir(III) catalyst from the Ir(II) state by molecular oxygen, resulting to $O_2^{\bullet-}$ formation (iii) The generated $O_2^{\bullet-}$ then accepts electron and H^+ from $NADH^{\bullet+}$ to generate H_2O_2 and NAD^+.[12]

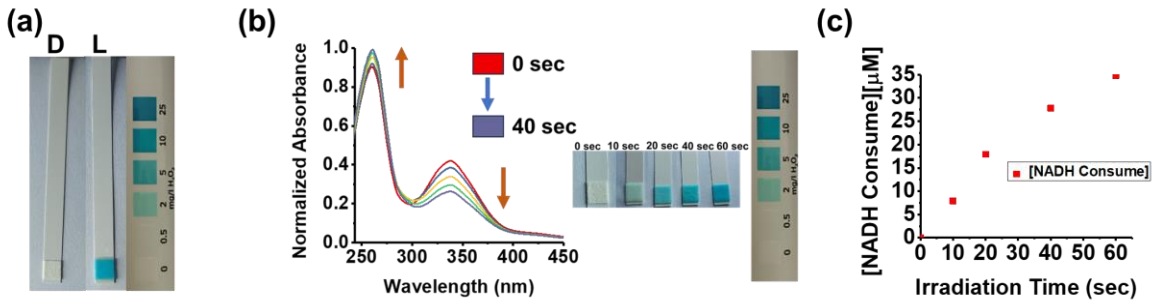

Figure 3.12: (a) Detection of H_2O_2 generation after irradiation of 1 min (Light source: 525 nm, 50.2 J cm^{-2}) for the reaction of photocatalyst **6** (2 μM) with NADH (240 μM) in 0.5% DMSO/99.5% PBS (v/v). (b) Detection of H_2O_2 generation after irradiation of various time intervals (Light source: 525 nm, 50.2 J cm^{-2}) for the reaction of photocatalyst **6** (2 μM) with NADH (260 μM) in 0.5% DMSO/99.5% PBS (v/v). The experiment was repeated three times independently. The outcome of the results was expressed as mean ± SD. (c) The concentration of NADH consumed vs irradiation time plot for **6** (2 μM) upon 525 nm light (50.2 J cm^{-2}) irradiation in 0.5% DMSO/99.5% PBS (v/v) solution.

Table 3.4: Comparison of TON and TOF of **4-6** with other reported Ir(III) photo-catalysts for NADH photo-oxidation.

Photocatalysts	TON	TOF (h^{-1})
4[a]	17.0±2.5	621.4±90.6
5[a]	28.0±2.1	841.4±45.8
6[a]	66.9±1.6	1003.5±24.6
1[b]	101.5±4.3	609.2±25.6
2[b]	83.2±4.4	499.1±26.5
3[b]	116.2±4.4	697.4±26.4
Ir1[c]	16.8	33.6
Ir8[d]	21.1	126.4
Ir9[d]	122.5	735.1
Ir12[e]	18.0	270.6
Ir23[f]	8.4	16.9
Ir24[f]	21.4	42.8
Ir25[f]	207.1	414.2

Ce6[f]	24.5	49.0

[a]TON and TOFs of **4-6** (2 μM each) for photocatalytic oxidation of NADH (240 μM) in 0.5% DMSO and 99.5% PBS solution, light source: 525 nm, 50.2 J cm^{-2}. [b]TON and TOFs for photocatalytic oxidation of NADH (175 μM) by **1-3** (1 μM each) in DMSO:PBS (1:99, v/v) solution, light source: 400-700 nm, 10 J cm^{-2}. [c]TON and TOFs for photocatalytic NADH oxidation (120 μM) by **Ir1** (3 μM) in 0.5% DMSO and 99.5% PBS, light source: 463 nm, 8.9 J cm^{-2} (Taken from reference 12). [d]TON and TOFs for photocatalytic oxidation of NADH by **Ir8** and **Ir9** (1 μM each) in PBS, light source: 525 nm, 29.56 J cm^{-2} (Taken from reference 14). [e]TON and TOFs for photocatalytic oxidation of NADH (100 μM) by **Ir12** (5 μM) in water, light source: 635 nm, 145 mW cm^{-2} (Taken from reference 7). [f]TON and TOFs for photocatalytic oxidation of NADH (160 μM) by **Ir23**/**Ir24**/**Ir25**/**Ce6** (5 μM each) in PBS, light source: 465 nm, 1.2 J cm^{-2} (Taken from reference 17).

3.3.7. In Solution ROS Generation

Ir(III) photocatalysts are known to generate $^1O_2$ on exposure to light *via* the type II mechanism.[3,4,12,14] $^1O_2$ generation tendency of photocatalysts **4-6** was studied by monitoring the change in absorbance of the $^1O_2$ probe, 1,3-diphenylisobenzofuran (DPBF),[19,20] under exposure to green light (for the theory of DPBF, see **Chapter II**, **section 2.3.4**). The decrease in the absorbance of DPBF in the presence of **4-6** under green light irradiation indicated $^1O_2$ generation tendency (Figures 3.13a-c). The reference photocatalyst $[Ru(bpy)_3]Cl_2$ also showed similar behaviour under green light irradiation (Figure 3.13d). The $^1O_2$ generation

tendency of photocatalysts increased with an increase in the irradiation time, as was evident from the change in the absorption *vs.* irradiation time plot (Figure 3.13e). Furthermore, the quantum yield of photocatalysts **4-6** for $^1O_2$ generation was 0.23, 0.24, and 0.26, respectively, which is higher than the reference photocatalyst $[Ru(bpy)_3]Cl_2$ (quantum yields $\Phi_\Delta = 0.22$ in 0.5% DMSO and 99.5% PBS, v/v) (Figure 3.13d). Additionally, we conducted control experiments to confirm the necessity of both light and the **4-6** for ROS generation (Figures 3.14a-c).

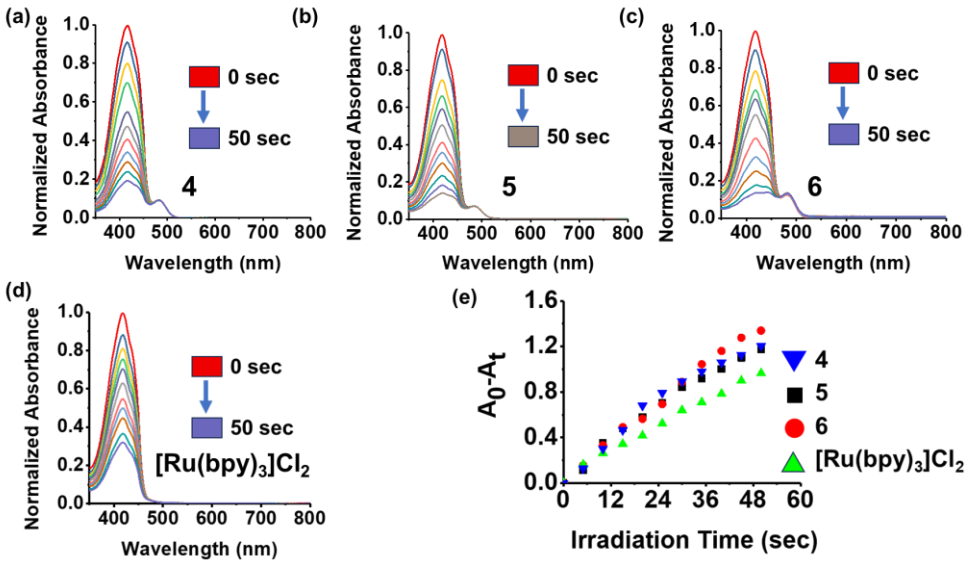

Figure 3.13: (a), (b) and (c) and (d) represent $^1O_2$ generation by photocatalysts **4**/**5**/**6**/$[Ru(bpy)_3]Cl_2$ (2 μM each), respectively, in a 0.5% DMSO/99.5% PBS (v/v) solution as was detected with DPBF (50 μM) and monitored by UV-Vis. spectroscopy upon irradiation with 525 nm light (50.2 J cm^{-2}) at different time intervals. (e) Change in absorbance *vs.* irradiation time plot for **4-6**, and reference $[Ru(bpy)_3]Cl_2$ (2 μM each) upon 525 nm light (50.2 J cm^{-2}) irradiation in 0.5% DMSO/99.5% PBS (v/v) solution.

When a DPBF solution was treated with **6** (the most active one) under dark, the absorbance remained almost unchanged (Figure 3.14a), verifying that $^1O_2$ production resulted from **4**/**5**/**6**+Light. This observation suggested that the photocatalysts could act as good photosensitizers for PDT applications. Further, the tendency of the photocatalysts to generate hydroxyl radical (•OH) was examined by the methylene blue probe under green light exposure (525 nm, 50.2 J cm^{-2}).[21] When the methylene blue + **4/5/6** in a solution of 0.5% DMSO + 99.5% PBS was exposed to light, the methylene blue-based absorbance between 650-700 nm was decreased with time (Figures 3.14b-d), indicating the •OH generation tendency of the photocatalysts. Thus, **4-6** would show photocytotoxicity via type I (NADH oxidation, H_2O_2, and •OH generation) and type II ($^1O_2$ production) pathways. This is a novel observation, as most of the Ir(III) or Ru(II) based photosensitizers are reported to show anticancer activity by the type II pathway.[22-24]

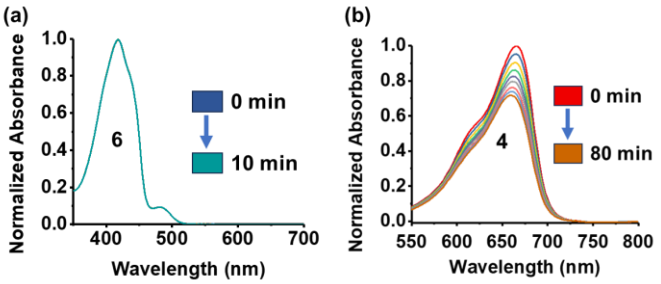

Figure 3.14: (a) Absorption spectra of DPBF (50 µM) in the presence of **6** (2 µM) in 0.5% DMSO/99.5% PBS (v/v) under dark conditions. (b) represent •OH generation by photocatalysts **4** (2 µM) in a 0.5% DMSO/99.5% PBS (v/v) solution as was detected with methylene blue (15 µM) and monitored by UV-Vis. spectroscopy upon irradiation with 525 nm light (50.2 J cm^{-2}) at different time intervals.

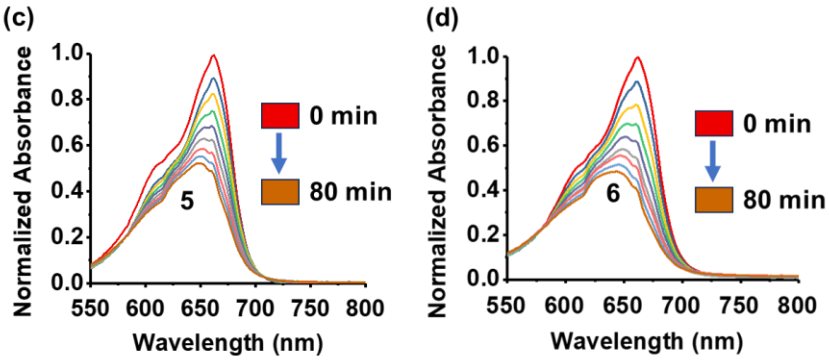

Figure 3.14: (c) and (d) represent ˙OH generation by photocatalysts **5** and **6** (2 μM each), respectively, in a 0.5% DMSO/99.5% PBS (v/v) solution as was detected with methylene blue (15 μM) and monitored by UV-Vis. spectroscopy upon irradiation with 525 nm light (50.2 J cm^{-2}) at different time intervals.

3.3.8. Photo-Cytotoxicity

The excellent ROS generation and photocatalytic (NADH oxidation) activities of **4-6** prompted us to investigate the anticancer potential of photocatalysts against various cancer cell lines after light exposure. The cytotoxic potential of photocatalysts **4-6** was studied against A549 and HeLa cancer cell lines (Figures 3.15a–f), under both dark and light irradiation (10 J cm^{-2}, 400-700 nm). The IC_{50} values in dark and light under normoxic conditions are presented in Table 3.5. As per the results, the light toxicity of photocatalysts **4-6** in the above cell lines was significantly higher than their dark toxicity. Specifically, under light irradiation, photocatalysts **4-6** showed cancer cell killing abilities with extremely low micromolar IC_{50} values (Table 3.5). Photocatalyst **6** demonstrated the highest photocytotoxicity with IC_{50} < 1.0 μM against both cancer cell lines (Table 3.5). PIs (Dark

IC_{50}/Light IC_{50}) of these photocatalysts were also in the range of > 20-71. Together, the above results confirmed the phototoxic nature of photocatalysts **4-6** (Table 3.5). Additionally, photocatalyst **6** exhibited comparable phototoxicity against A549 cancer cells to the previously reported Ir(III)-based photocatalyst **Ir23** (Table 3.5).[17] Photocatalyst **6** also demonstrated significantly higher phototoxicity than other previously reported Ir(III)-based

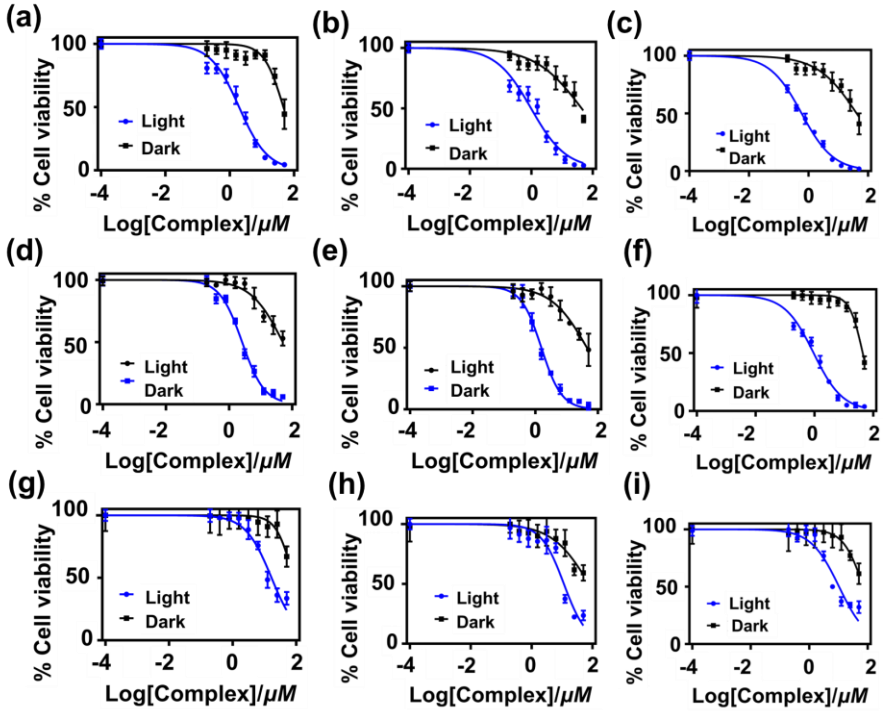

Figure 3.15: (a–c) Cell viability plots for photocatalysts **4**–**6** in A549, (d–f) HeLa, and (g–i) BEAS-2B cells following 4 h of incubation. In each case, one set of cells was exposed to visible light (400–700 nm, 10 J cm^{-2}) for 1 h, while the other set was kept in the dark. Blue and black plots represent light-exposed and dark, respectively. The outcome of the results was expressed as mean ± SD (error bars are standard deviations) of the three independent repeated experiments. The statistical analysis was done by One-way ANOVA followed by Tukey's Post Hoc Test (n=3).

photocatalysts, such as **Ir1**, **Ir21**, **Ir24,** and **Ir25** (Table 3.5).[12,16,17] The IC_{50} value of photocatalyst **6** against A549 cancer cells under light irradiation was significantly lower than that of the clinically used photosensitizers 5-ALA and cis-platin.[12] Additionally, under light irradiation, photocatalyst **6** demonstrated superior cytotoxicity against A549 cells, with an IC_{50} value lower than those of photocatalyst **1** (2.2±0.5 μM) and **2** (1.8±0.2 μM), as reported in **Chapter II**. Moreover, its activity was also higher than that of photocatalyst **3** (IC_{50} = 0.8±0.1 μM) as reported in **Chapter II**, further underscoring the therapeutic potential of **6** under photoactivation. To evaluate the safety of photocatalysts **4-6** toward healthy cells, we measured their cytotoxicity against normal human bronchial epithelial BEAS-2B cells (Figures 3.15g–i). All three photocatalysts (**4-6**) showed IC_{50} values > 50 μM, indicating negligible toxicity (Table 3.5). These photocatalysts exhibited a selectivity index (SI) > 6-19, which indicated their high selectivity towards cancer cell lines. Further, for comparison, cisplatin's toxicity toward BEAS-2B cells was studied by MTT assay (Figure 3.16).[25,26] The obtained dark and light (10 J cm^{-2}, 400-700 nm) IC_{50} values were 20.4 ± 1.6 μM and 23.4± 2.4 μM, respectively (Table 3.5). These data demonstrated that photocatalysts **4-6** possess a markedly safer profile toward healthy cells than cisplatin. Further, the sulforhodamine B (SRB) assay was also performed against A549 cells to validate the MTT assay results (Figures 3.17a, b). **5** exhibited IC_{50} values of 45.9±3.2 μM in the dark and 0.9±0.3 μM under light (Table 3.6). **6** showed IC_{50} values of 42.1±2.7 μM in the dark and 0.7±0.1 μM under light (Table 3.6). Interesting to note that a similar result was also obtained with the MTT assay. Since photocatalyst **6** was more active than **5**, all future mechanistic

studies were performed with only photocatalyst **6**. It is well established that photocatalysts that show NADH oxidation can also show anticancer activity in hypoxia.[12,16] Therefore, we explored the photoinduced anticancer activity of photocatalysts **5** and **6** against A549 cancerous cells under hypoxic conditions (1% O_2) (Figures 3.17c, d). Again, **6** demonstrated the highest photocytotoxicity (IC_{50} = 1.7±0.1 μM) than photocatalyst **5** (IC_{50} = 3.3±0.1 μM) (Table 3.7). The photocytotoxicity of the photocatalyst in hypoxia is almost 4 times lower than that of normoxia. The reason behind this is the decrease in $^1O_2$ generation due to the very low availability of oxygen.

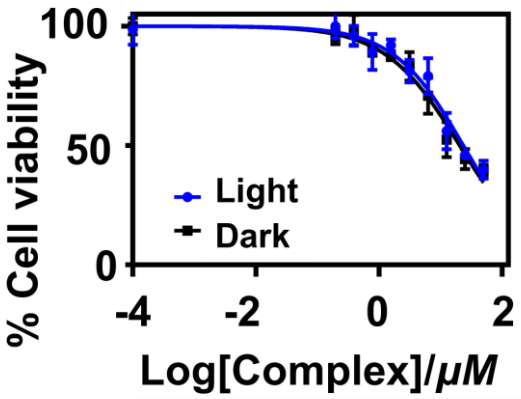

Figure 3.16: Cell viability plots for Cisplatin in normal human bronchial epithelial BEAS-2B cells after 4 h incubation. One set of cells was exposed to visible light (400-700 nm, 10 J cm^{-2}) for 1 h while the other set was kept in the dark. Blue and black plots represent light-exposed and dark, respectively. The outcome of the results was expressed as mean ± SD (error bars are standard deviations) of the three independent repeated experiments. The statistical analysis was done by One-way ANOVA followed by Tukey's Post Hoc Test (n=3).

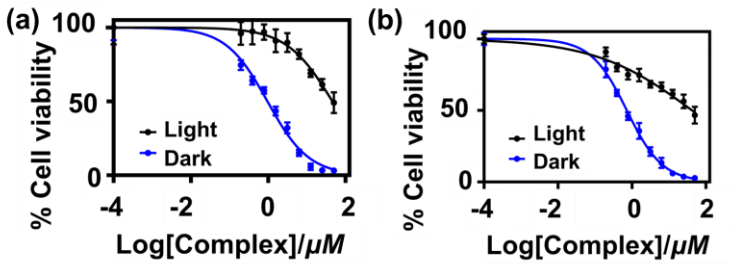

Figure 3.17: Cell viability plots using sulforhodamine B (SRB) assay for photocatalysts (a) **5** and (b) **6** in A549 cells. Experimental conditions: 4 h incubation. The outcome of the results was expressed as mean ± SD. The statistical analysis was done by One-way ANOVA followed by Tukey's Post Hoc Test (n=3).

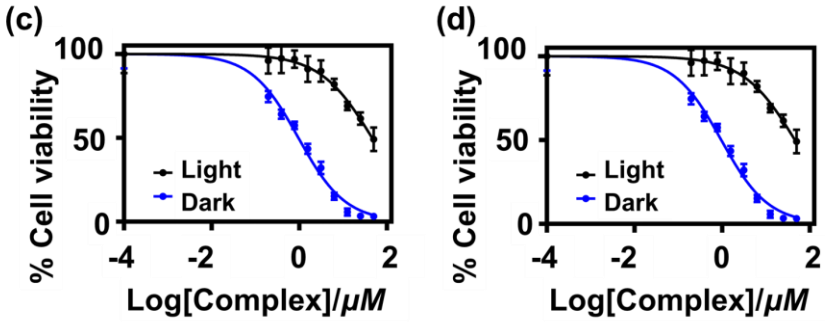

Figure 3.17: Cell viability plots for photocatalysts (c) **5** and (d) **6** under hypoxic conditions in A549 cells. Experimental conditions: 4 h incubation. One set of cells was exposed to visible light (400-700 nm, 10 J cm^{-2}) for 1 h while the other set was kept in the dark. blue and black plots represent light-exposed and dark, respectively. The outcome of the results was expressed as mean ± SD (error bars are standard deviations) of the three independent repeated experiments. The statistical analysis was done by One-way ANOVA followed by Tukey's Post Hoc Test (n=3).

Table 3.5: IC_{50} (μM) values of **4-6** and some selected Ir(III)-based photo-catalysts under normoxia.

Photoc-atalyst	A549				HeLa				Beas 2B	
	Dark	Light	PI	SI	Dark	Light	PI	SI	Dark	Light
4[a]	46.5± 1.3	1.9±0.1	23.8	8.5	>50.0	2.5± 0.1	>20. 0	6.7	> 50.0	16.6 ±1.2
5[a]	43.2 ±1.7	0.9± 0.1	44.1	11.7	44.4± 2.1	1.6± 0.1	27.8	7.1	> 50.0	11.4 ±1.3
6[a]	41.2± 1.5	0.6±0.1	71.0	18.0	43.7± 1.8	0.9± 0.1	47.0	11.2	> 50.0	10.4 ±1.8
1[b]	> 25.0	2.2±0.5	> 11 .3							
2[b]	> 25.0	1.8±0.2	>13. 8							
3[b]	> 25.0	0.81±0. 1	30.9							
Ir1[c]	43.6± 2.5	1.6±0.1	71.0		35.4± 1.9	1.9± 0.3	18.6			

Ir21[d]	98.6±4.8	49.3±0.7	2.0							
Ir22[d]	>100.0	>100.0	NA							
Ir23[e]	>100.0	18.6±0.2	>5.4							
Ir24[e]	37.5±1.2	0.9±0.0	41.7							
Ir25[e]	55.0±1.3	0.2±0.0	275							
5-ALA[c]	>10000	>10000	NA	NA	>10000	2510±280	>4.0	NA	NA	NA
cis-platin[c]	8.3±1.2	8.6±0.9	NA	2.7	7.1±0.8	6.0±0.5	1.2	3.9	20.4±1.6	23.4±2.4

[a]Cells were incubated with **4**-**6** for 4 h, followed by light exposure (400–700 nm, 10 J cm^{-2}) over 1 h. Recovery after irradiation: 43 h. For the dark group, the light irradiation step was absent. [b]Cells were incubated with **1**-**3** for 6 h, followed by light exposure (400–700 nm, 10 J cm^{-2}) over 2 minutes. Recovery after irradiation: 18 h. For the dark group, the light

irradiation step was absent. [c]Cells were incubated with **Ir1** for 2 h, followed by light exposure (465 nm, 8.9 J cm^{-2}) over 30 min. Recovery after irradiation: 46 h. For the dark group, the light irradiation step was absent (adopted from reference 12). [d]Cells were incubated with **Ir21/Ir22** for 4 h, followed by light exposure (400-700 nm, 17.2 J cm^{-2}) over 30 min. Recovery after irradiation: 44 h. For the dark group, the light irradiation step was absent (adopted from reference 16). [e]Cells were incubated with **Ir23/Ir24/25/5-ALA/cis-platin** for 4 h, followed by light exposure (465 nm, 11.7 J cm^{-2}) over 5 min. Recovery after irradiation: 32 h. For the dark group, the light irradiation step was absent (adopted from reference 17).

Table 3.6: IC_{50} values of **5** and **6** against A549 cancer cells determined by SRB assay.

Photocatalyst	Dark	Light
5	45.9±3.2	0.9±0.3
6	42.1±2.7	0.7±0.1

White light irradiation (400−700 nm, 10 J cm^{-2}). Light treatment: Incubation time: 4 h, Total irradiation = 10 J cm^{-2} over 1 h. Recovery time: 43 h. Dark treatment: Incubation time: 4 h, Recovery time: 43 h.

Table 3.7: IC_{50} (μM) values of **5** and **6** under hypoxic conditions (1% O_2).

Photocatalyst	A549		
	Dark	Light	PI

5	54.6±2.3	3.3±0.1	16.3
6	51.8±1.1	1.7±0.1	30.2

White light irradiation (400−700 nm). Light treatment: Incubation time: 4 h, Total irradiation = 10 J cm^{-2} over 1 h. Recovery time: 43 h. Dark treatment: Incubation time: 4 h, Recovery time: 44 h.

3.3.9. Cellular Localization

Cellular uptake and localization of photosensitizers are crucial to understand their anticancer mechanism.[3,4,11] photocatalyst **6** exhibited a green fluorescence due to the presence of the coumarin 6 moiety. This fluorescence property prompted us to explore the cellular uptake and localization by confocal imaging.[3,4] Hoechst dye and Mitotracker Red (MTR) dye were used to probe the cell's nucleus and mitochondria, respectively.[27,28] Notably, A549 cells treated with photocatalyst **6** showed green fluorescence, as represented by the photocatalyst **6** panel of Figure 3.18, that confirmed the cellular uptake of **6** within 4 h. The merged panel of Hoechst dye and **6** in Figure 3.18 clearly indicated the cytoplasmic localization of photocatalyst **6**. Moreover, the merged panel of MTR dye and **6** revealed that photocatalyst **6** primarily accumulated within mitochondria (PCC value = 0.68) of A549 cells (as depicted in Figure 3.18). Mitochondria play an essential role in cellular energy generation and are crucial for cell survival.[27,28] The mitochondrial ETC is closely associated with the ATP generation process, and NADH is an important and essential constituent of mitochondrial ETC.[29] We have shown the high efficiency of photocatalyst **6** in catalytic NADH photo-

oxidation (*vide supra*). Thus, photocatalyst **6** can oxidize NADH in mitochondria on light exposure, like other reported Ir(III)-based photo-catalysts (e.g, **Ir1**, **Ir8**, **Ir9**, **Ir25**, **etc**.) to create metabolic disorder.[12,14,17]

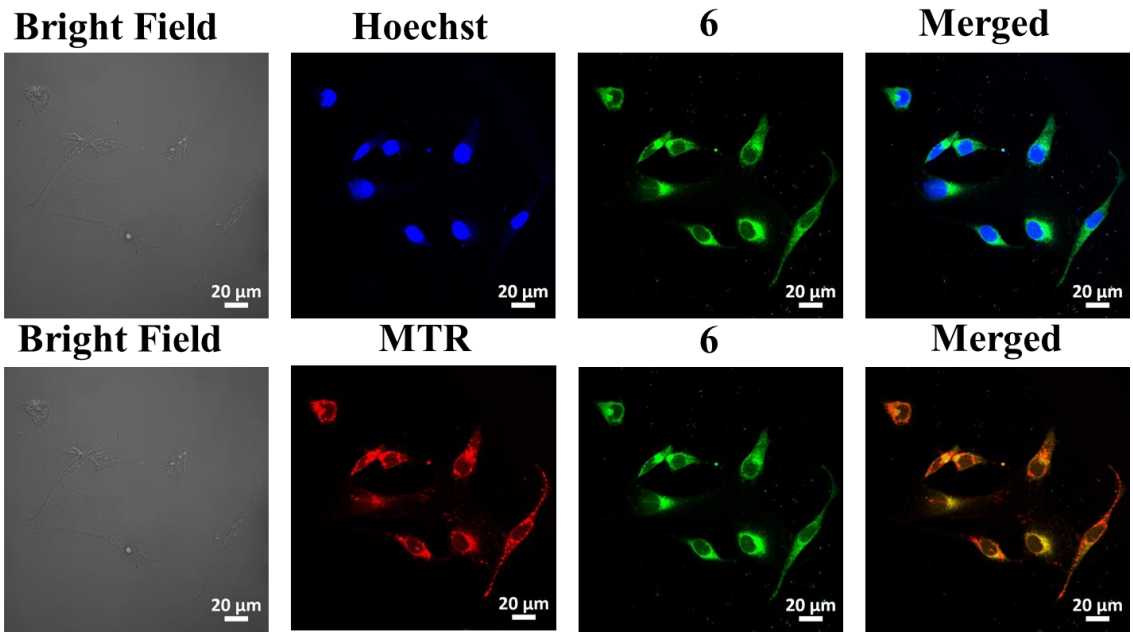

Figure 3.18: Cellular localization study of photocatalyst **6** in A549 cancer cells. A549 cells were incubated with 30 µM photocatalyst **6** for 4 h, followed by co-staining with Hoechst dye (5 µg/mL) or MitoTracker dye (250 nM) (L = Light, D = Dark). Under the following conditions, confocal images were recorded: blue emission of nucleus staining dye Hoechst (λ_{ex}~405 nm, λ_{em}~460-475 nm), red emission of MTR (λ_{ex}~630 nm, λ_{em}~650-665 nm), green emission of **6** (λ_{ex}~488 nm, λ_{em}~500-520 nm). Scale bar: 20 µm. The experiment was repeated three times independently with similar results.

3.3.10. In-cell NADH Oxidation

As discussed previously, photocatalyst **6** facilitated the photooxidation of NADH under a cell-free system. In order to validate this observation under cellular conditions, the effect of photocatalyst **6** (25 μM) treatment on the levels of NAD^+ and NADH was monitored in A549 cells under dark and light irradiation conditions. The results indicated that in the dark, photocatalyst **6** did not cause any significant change in the ratio of NAD^+ and NADH as

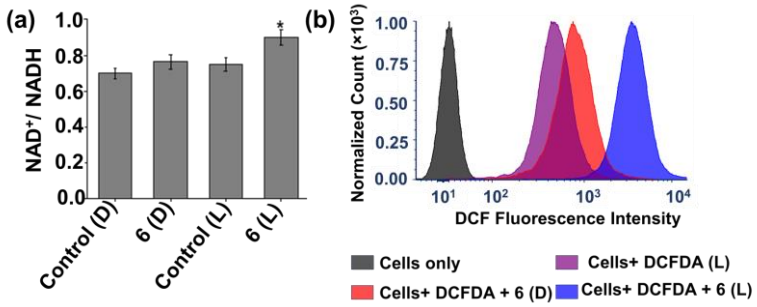

Figure 3.19: (a) The plot shows the ratio of NAD^+ and NADH in A549 cells treated with photocatalyst **6** (25 μM) through spectrophotometric analysis. One set of cells was exposed to visible light (400-700 nm, 10 J cm^{-2}) after 4 h of incubation with photocatalyst **6**, while the other set was kept continuously in the dark. The total incubation period following the addition of the photocatalyst was 24 h. The results are presented as mean ± SEM. * $p< 0.05$ as compared to the dark and light control groups by Student's T-test (L = Light, D = Dark). (b) Intracellular generation of ROS in A549 cells induced by **6** (1 μM) using DCFH-DA probe (L = Light, D = Dark). Incubation time with **6**: 4 h, Light irradiation (400-700 nm, 10 J cm^{-2}) for 1 h. Recovery after irradiation: 4 h. For the dark group, the light irradiation step was absent. The experiment was repeated three times independently with similar results.

compared to the untreated control group (Figure 3.19a). The only light irradiation also did not show any significant change in the ratio of NAD^+ and NADH as compared to the untreated dark control group (Figure 3.19a). However, photocatalyst **6** treatment in the presence of light led to a statistically higher ratio of NAD^+ and NADH as compared to the untreated light control group (Figure 3.19a). Thus, it clearly suggested the ability of photocatalyst **6** to photo-oxidize NADH within cells. It is important to discuss that researchers have mostly reported NADH photo-oxidation in solutions and have correlated in-solution NADH oxidation efficiency with anticancer activity.[3,4] To the best of our knowledge, this was the 2nd time (after Ref. 12) that in-cell NADH photo-oxidation has been confirmed with any photocatalyst.

3.3.11. In-cell ROS Generation

In an aqueous solution, in the absence of NADH, photocatalyst **6** produced $^1O_2$ on light exposure via a type II pathway, whereas in the presence of NADH+Light, **6** also produced H_2O_2 (Figures 3.12a, b) via a type I pathway. Thus, this photocatalyst can show PDT activity through a combined pathway of type I + type II and ultimately could produce excessive ROS in cells.[3,4,12,14] Therefore, the intracellular ROS generation tendency of photocatalyst **6** was examined by DCFH-DA assay (for the theory of DCFH-DA assay, see **Chapter II**, **section 2.3.6**).[30,31] As depicted in Figure 3.19b, when A549 cells were treated with **6** (1 μM) in the absence of light, there was a 1.6-fold increase in the DCF intensity. However, there was a 12-fold enhancement in the intensity of DCF in the presence of light. This indicated the light-induced ROS generation potential of photocatalyst **6** within the A549 cancerous cells. As

photocatalyst **6** was mainly located within cells' mitochondria, therefore, we hypothesized that it might induce oxidative stress in mitochondria, leading to mitochondrial depolarization followed by cell apoptosis.[4]

3.3.12. Change in Mitochondrial Membrane Potential and Cellular Apoptosis

Photocatalyst **6**, localized in the mitochondria and producing ROS upon exposure to visible light, may depolarize mitochondria after light irradiation. The JC-1 assay was used to explore the effects of photocatalyst **6** on mitochondrial membrane potential (for the theory of the JC-1

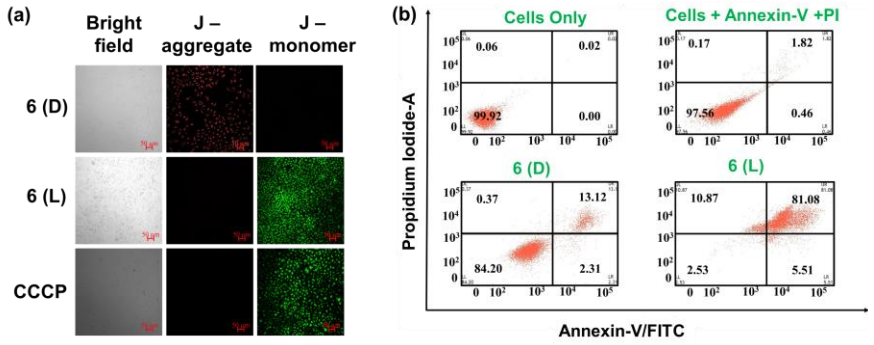

Figure 3.20: (a) Change in MMP by photocatalyst **6** (1 μM) treated A549 cells as monitored by JC-1 assay (L = Light, D = Dark). Incubation time with **6**: 4 h, Light irradiation (400-700 nm, 10 J cm^{-2}) for 1 h. Recovery after irradiation: 6 h. For the dark group, the light irradiation step was absent. Scale bar: 50 μm. CCCP was used as the positive control. (b) Apoptotic death of A549 cells induced by **6** (1 μM) under light irradiation (400-700 nm, 10 J cm^{-2}) was detected by annexin V-FITC/propidium iodide (PI) assay (L = Light, D = Dark). Incubation time with **6**: 4 h, Light irradiation (400-700 nm, 10 J cm^{-2}) for 1 h. Recovery after irradiation: 43 h. For the dark group, the light irradiation step was absent. For both (a) and (b), the experiment was repeated three times independently with similar results.

assay, see **Chapter II,** section **2.3.7**).[32,33] When A549 cells were exposed to photocatalyst **6** (1 μM) under dark conditions, they exhibited red fluorescence (Figure 3.20a) due to JC-1 in its aggregate form, suggesting intactness of mitochondrial membrane potential and low/negligible dark toxicity of **6**. Whereas, after light exposure, these cells showed a green fluorescence signal (Figure 3.20a), suggesting the conversion of JC-1 into its monomeric form and hence mitochondrial depolarization. The positive control CCCP also produced a similar response (Figure 3.20a).

Mitochondrial depolarization is widely recognized as a hallmark of cell apoptosis.[34] To identify the type of cell death induced by **6** (1 μM)+Light, Annexin V-FITC/propidium iodide (PI) assay was carried out by FACS analysis (Figure 3.20b).[34] The annexin V-FITC/PI assay can precisely differentiate cell populations into various cell death types.[34] When A549 cells were treated with **6** (1 μM) in the absence of light, only *ca.* 15% apoptotic (Annexin V^{+ve} PI^{-ve} and Annexin V^{+ve} PI^{+ve}) cells were found. The percentage of apoptotic (Annexin V^{+ve} PI^{-ve} and Annexin V^{+ve} PI^{+ve}) cells was increased to 87% after light exposure.

The apoptotic cell death pathway is mediated through the final effector protein caspase 3.[35,36] Therefore, the activity of caspase 3 was monitored by treating A549 cells with **6** (25 μM) under dark and light exposure conditions (Figure 3.21). The result indicated that treatment of photocatalyst **6** under dark conditions led to only a marginal increase in the caspase 3 activity as compared to control cells (Figure 3.21). However, similar treatment on light exposure resulted in a significantly higher increase in caspase activity than in dark

conditions (Figure 3.21). These findings thus clearly indicate that photocatalyst **6** induced cellular apoptosis via ROS-triggered mitochondrial depolarization.

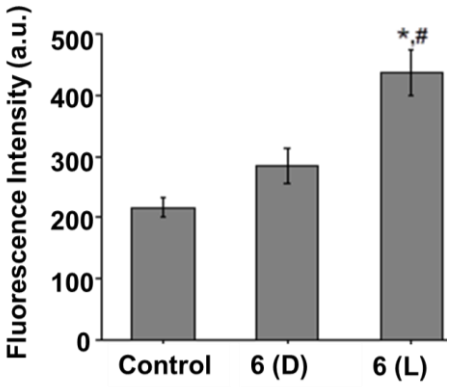

Figure 3.21: The plot shows the activity levels of caspase 3 in A549 cells treated with photocatalyst **6** (25 μM) through spectrofluorometric analysis (L = Light, D = Dark). Incubation time with **6**: 4 h, Light irradiation (400-700 nm, 10 J cm^{-2}) for 1 h. Recovery after irradiation: 48 h. For the dark group, the light irradiation step was absent. The results are presented as mean ± SD. * $p< 0.05$ as compared to the control group by Student's T-test (n=3). # $p<0.05$ as compared to dark conditions by Student's T-test .

3.4. Conclusion

Herein, we have successfully synthesized and characterized three Ir(III)-based photocatalysts. The light-induced anticancer potential of photocatalysts was enhanced by extending the conjugation within the ligand (e.g., phen *vs* dppz *vs* aip). The absorption spectra of photocatalysts **4-6** showed a coumarin 6-based band between 450-550 nm, and an MLCT band between 400-450 nm, which were used to achieve green light-induced catalytic

NADH oxidation and visible light-induced anticancer activity. **6** turned out to be a highly efficient photocatalyst for NADH oxidation in an aqueous solution with a turnover number of *ca.* 66.9±1.6 and a TOF of *ca.* 1003.5±24.6 h^{-1}. Meanwhile, **4** and **5** had TON *ca*. 17.0±2.5 and 28.0±2.1, respectively, and exhibited TOF *ca*. 621.4±90.6 h^{-1} and 841.4±45.8 h^{-1}, respectively. Thus, extended conjugation in **6** increases the electron-accepting capability of **6** than **4** and **5**. The catalytic activity of photocatalyst **6** was much higher than the previously reported Ir(III) photocatalysts, **Ir1**, **Ir8**, **Ir23**, and **Ir24**.[12,14,17] Most of the research based on photocatalytic therapy showed in solution NADH oxidation and correlated their efficiency with anticancer activity.[3,4] This is the 2nd time in-cell NADH photo-oxidation was achieved with any catalysts, validating the concept of photocatalytic cancer therapy. The cellular localization study of the green fluorescent photocatalyst **6** in A549 cancer cells showed that **6** primarily accumulated within the mitochondria. **4-6** showed significantly higher toxicity in A549 and HeLa cancer cells than normal human bronchial epithelial BEAS-2B cells under light conditions. photocatalysts **4-6** demonstrated remarkably low micromolar photo-cytotoxicities against cancer cells in both normoxia and hypoxia. PI values (Dark IC_{50}/Light IC_{50}) of these photocatalysts were also high, in the range of >20-71. **6** had a higher phototoxicity than **4** and **5**, as well as photocatalysts reported in **Chapter II**, which could be due to more extended conjugation. The higher extended π-conjugation in **6** might enhance its lipophilicity, intracellular uptake, and photosensitivity.[4,16,17] The apoptotic photo-activated anticancer activity of these photocatalysts in normoxia mainly arises from their ability to generate ROS and oxidize NADH in-cell on light exposure, which in turn activates caspase 3. So far, in photocatalytic cancer therapy under normoxia, photocatalysts are

reported to show anticancer activity through the combined effects of NADH oxidation and $^1O_2$ generation. But here, **4-6** not only generated $^1O_2$ and oxidized NADH but also generated $^{\cdot}OH$ radicals.

3.5. Experimental Section

3.5.1. Materials and General Instrumentation

Coumarin 6 was purchased from E. Merck India Pvt. Ltd., tetrabutylammonium hexafluorophosphate were purchased from BLD Pharma. dppz was prepared following a literature procedure using 1,10-phenanthroline-5,6-dione as a precursor.[37,38] The details of the remaining materials are provided in **Chapter II** (**section 2.5.1**).

3.5.2. Synthesis of Ir(III) *μ*-chloro-Bridged Dimer

$[Ir(CO6)_2Cl]_2$ dimer was prepared using a previously reported method with slight modifications.[4,5] Under dark conditions, 1 equiv. of $IrCl_3.xH_2O$ and 2 equiv. of coumarin 6 were dissolved in a mixture of 2-ethoxyethanol and water (Total 16 mL; 3:1 v/v) (Scheme 3.1). The reaction mixture was refluxed at 115 °C for 24 h. After cooling to room temperature, the precipitate

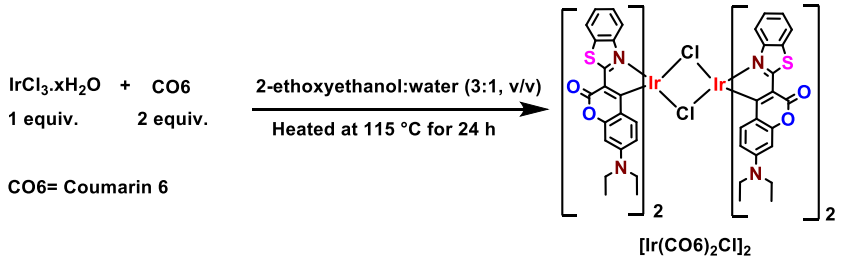

Scheme 3.1: Synthetic scheme of $[Ir(CO6)_2Cl]_2$.

was filtered off and washed with diethyl ether. The orange solid Ir(III) μ-chloro-bridged dimer was obtained.

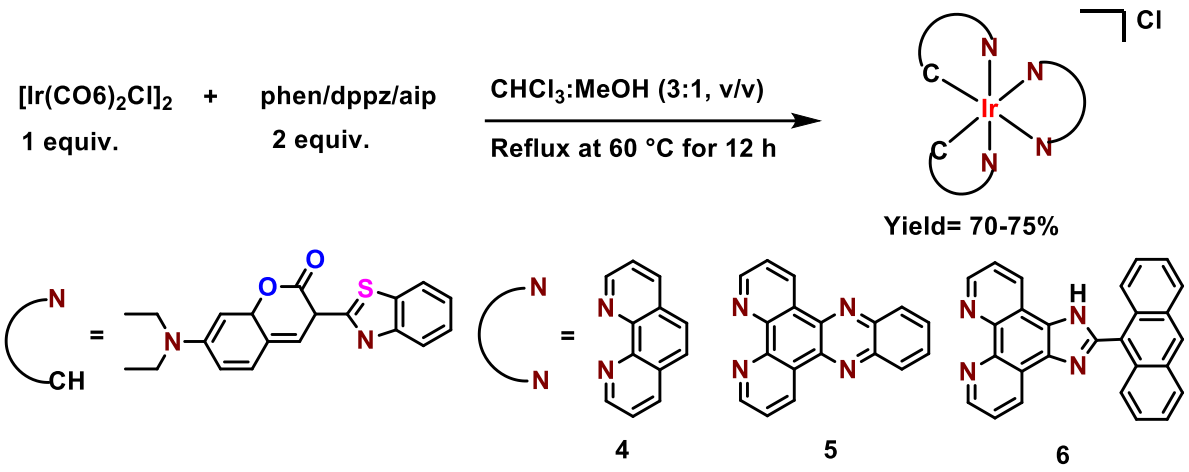

Scheme 3.2: Synthetic scheme of **4-6**.

3.5.3. Synthesis of 4-6

To synthesize the photocatalysts **4-6**, 1 equiv. of $[Ir(CO6)_2Cl]_2$ dimer and 2 equiv. of N,N donor ligand (phen/dppz/aip) were dissolved in 20 mL of $CHCl_3$/MeOH (3:1; v/v) (Scheme 32). The reaction mixture was refluxed at 60 °C for 12 h. After cooling to room temperature, the solvent was removed under reduced pressure. The resulting solids were extracted with DCM and water. Finally, Na_2SO_4 was added to the above extracted DCM solution to remove any water content. The solvent was then removed under *vacuum* to afford the crude product. The crude product was purified by column chromatography on neutral alumina, eluted with methanol: n-hexane (1:99, v/v).

Photocatalyst **4:** Yield = 70 %, $C_{52}H_{42}ClIrN_6O_4S_2$ (MW = 1106.73): calcd. C = 56.43, H = 3.83, N = 7.59, exp. C = 56.61, H = 3.59, N = 7.38, UV−Vis. spectral data were recorded in DMSO where λ_{max} = 482 nm ($\varepsilon = 1.2 \times 10^6$ M^{-1} cm^{-1}), 457 nm ($\varepsilon = 9.3 \times 10^5$ M^{-1} cm^{-1}), 394 nm ($\varepsilon = 2.18 \times 10^5$ M^{-1} cm^{-1}), $\lambda_{em\ max}$ = 504 nm. ^{1}H NMR (500 MHz, DMSO-d_6, ppm) δ: 9.22 (t, *J* = 4.8 Hz, 2H), 8.95 (d, *J* = 7.9 Hz, 2H), 8.22 (d, *J* = 8.6 Hz, 4H), 8.00 (d, *J* = 7.9 Hz, 2H), 7.11 (t, *J* = 7.5 Hz, 2H), 6.72 (t, *J* = 7.7 Hz, 2H), 6.51 (s, 2H), 6.08 (dd, *J* = 9.1 Hz, 4H), 5.60 (d, *J* = 8.4 Hz, 2H), 3.32 (m, *J* = 5.8 Hz, 8H), 0.96 (t, *J* = 6.3 Hz, 12H). ^{13}C NMR (125 MHz, DMSO-d_6, ppm) δ: 180.80, 178.05, 157.52, 155.17, 152.73, 147.81, 146.41, 141.21, 132.24, 131.08, 128.63, 127.52, 124.92, 122.18, 118.93, 115.07, 109.87, 96.74, 44.28, 12.81. HR-MS (m/z) $[M]^+$: calcd. = 1071.2338, obt. = 1071.2358.

Photocatalyst **5:** Yield = 75 %, $C_{58}H_{44}ClIrN_8O_4S_2$ (MW = 1208.83): calcd. C = 57.63, H = 3.67, N = 9.27, exp. C = 57.92, H = 3.81, N = 9.16, UV−Vis. spectral data were recorded in DMSO where λ_{max} = 485 nm ($\varepsilon = 1.29 \times 10^6$ M^{-1} cm^{-1}), λ_{max} = 457 nm ($\varepsilon = 9.44 \times 10^5$ M^{-1} cm^{-1}), λ_{max} = 386 nm ($\varepsilon = 3.42 \times 10^5$ M^{-1} cm^{-1}), λ_{max} = 362 nm ($\varepsilon = 3.40 \times 10^5$ M^{-1} cm^{-1}), $\lambda_{em\ max}$ = 494 nm. ^{1}H NMR (500 MHz, DMSO-d_6, ppm) δ: 9.74 (d, *J* = 7.8 Hz, 2H), 9.38 (d, *J* = 5.0 Hz, 2H), 8.39 (dd, *J* = 5.5 Hz, 2H), 8.30 (s, 2H), 8.09-8.00 (m, 4H), 7.09 (t, *J* = 7.6 Hz, 2H), 6.82 (t, *J* = 7.8 Hz, 2H), 6.50 (d, *J* = 8.2 Hz, 2H), 6.06 (dt, *J* = 8.4, 5.7 Hz, 4H), 5.84 (d, *J* = 8.5 Hz, 2H), 3.31 (s, 8H), 0.97 (t, *J* = 6.8 Hz, 12H). ^{13}C NMR (125 MHz, DMSO-d_6, ppm) δ: 180.11, 177.78, 157.60, 155.31, 153.76, 152.84, 149.17, 147.97, 142.49, 139.13, 137.56, 133.27, 131.16, 130.39, 130.07, 129.76, 127.94, 127.89, 122.20, 118.83, 115.67, 109.98, 96.82, 44.47, 12.80. HR-MS (m/z) $[M]^+$: calcd = 1173.2556, obt. = 1173.2549.

Photocatalyst **6:** Yield = 72%, $C_{67}H_{50}ClIrN_8O_4S_2$ (MW = 1322.98): calcd. C = 60.83, H = 3.81, N = 8.47, exp. C = 61.05, H = 3.78, N = 8.53, UV−Vis. spectral data were recorded in DMSO where λ_{max} = 484 nm ($\varepsilon = 1.61 \times 10^6$ M^{-1} cm^{-1}), λ_{max} = 457 nm ($\varepsilon = 1.11 \times 10^6$ M^{-1} cm^{-1}), λ_{max} = 395 nm ($\varepsilon = 5.46 \times 10^5$ M^{-1} cm^{-1}), λ_{max} = 371 nm ($\varepsilon = 5.08 \times 10^5$ M^{-1} cm^{-1}), $\lambda_{em\ max}$ = 495 nm. ^{1}H NMR (500 MHz, DMSO-d_6, ppm) δ: 9.23 (s, 4H), 9.01 (dd, *J* = 5.2 Hz, 1H), 8.89 (s, 1H), 8.30 – 8.21 (m, 4H), 8.05 (d, *J* = 7.8 Hz, 2H), 7.72 (d, *J* = 8.0 Hz, 2H), 7.56 (d, *J* = 7.0 Hz, 2H), 7.46 (s, 2H), 7.15 (t, *J* = 7.4 Hz, 2H), 6.84 (t, *J* = 7.5 Hz, 2H), 6.52 (s, 2H), 6.07 (t, *J* = 9.4 Hz, 4H), 5.78 (d, *J* = 8.4 Hz, 2H), 3.12 (d, *J* = 8.7 Hz, 8H), 0.97 (s, 12H). ^{13}C NMR (125 MHz, DMSO-d_6, ppm) δ: 191.56, 178.15, 161.58, 157.59, 157.16, 156.29, 155.30, 152.74, 148.02, 134.73, 131.75, 131.03, 129.89, 127.74, 126.31, 124.89, 123.89, 122.04, 118.93,115.32, 44.27, 12.50. HR-MS (m/z) $[M]^+$: calcd = 1287.3026, obt. = 1287.2974.

3.5.4. Instruments

Instrumental details for UV-Vis., fluorescence, HRMS, multinuclear NMR, and FACS analysis are provided in **Chapter II** (**section 2.5.2**).

3.5.5. NMR Spectroscopy

The methods are provided in **Chapter II** (**section 2.5.7**).

3.5.6. UV-Vis. Spectroscopy

The method to record UV-Vis. Spectra are provided in **Chapter II** (**section 2.5.8**). Herein, the MeOH is used as a solvent system.

3.5.7. Fluorescence Spectra

The method to record fluorescence spectra of photocatalysts **4-6** (20 μM) in DMSO:H_2O (1:9, v/v) solution is given in **Chapter II** (**section 2.5.9**).

3.5.8. Photo-Stability of Photocatalysts

The method to study the photostability of photocatalysts **4-6** (2 μM) in DMSO:PBS (0.5:99.5, v/v) solution under light irradiation (525 nm, 50.2 J cm^{-2}) is given in **Chapter II** (**section 2.5.10**).

3.5.9. Single Crystal X-ray Crystallography

Single crystals of photocatalyst **4** were successfully obtained *via* the slow evaporation method in a solution of toluene: acetonitrile (1:1, v/v). Subsequently, a suitable crystal was carefully selected and securely mounted in a cryo loop utilizing a cryoprotectant oil. X-ray diffraction data for photocatalyst **4** were meticulously collected at 150 K temperature using a Bruker D8 Quest diffractometer, which was equipped with an Incoatec microfocus source (IμS 3.0 Mo K_α, λ = 0.710732 Å and a PHOTON-II CCD detector. The collected X-ray diffraction intensities were meticulously processed, integrated, and scaled utilizing APEX4 software. A multi-scan method with SADABS programming was employed to correct empirical absorption.[39] The structure was solved by intrinsic phasing with SHELXT[40] and refined by full-matrix least-square methods on F^2 using SHELXL using the ShelXle along with the Olex2 interface.[41,42] All non-hydrogen atoms underwent refinement with anisotropic displacement parameters, while hydrogen atoms were placed at calculated

positions and treated as riding atoms. For C-H bonds, the anisotropic displacement parameter was set at Uiso(H) = 1.2 Ueq(C). Molecular graphics, validation, and preparation of materials for the thesis were performed using ORTEP, Mercury, and public software tools, respectively. Details of crystal data collection and data refinement parameters are given in Table 2.8. **Deposition number: 2328794**.

Table 3.8: Selected crystallographic data for [Ir(CO6)$_2$(phen)]Cl (**4**)

Formula	$C_{104}H_{85}Cl_{1.8}Ir_2N_{12}O_8S_4$
Formula weight (g M^{-1})	2205.51
Temperature/K	150.00(10)
Crystal system	triclinic
Space group	P-1
a/Å	15.9979(3)
b/Å	19.7642(3)
c/Å	21.0712(3)
α/°	115.1910(10)
β/°	92.9290(10)

γ/°	96.2260(10)
Volume/Å^3	5958.08(17)
Z	2
ρ_{calc}g/cm^3	1.229
μ/mm^{-1}	2.392
F(000)	2210.0
Crystal size/mm^3	0.2 × 0.15 × 0.12
Radiation	Mo Kα (λ = 0.71073)
2Θ range for data collection/°	3.17 to 50
Index ranges	-19 ≤ h ≤ 19, -23 ≤ k ≤ 23, -25 ≤ l ≤ 25
Reflections collected	199000
Independent reflections	20957 [R_{int} = 0.1012, R_{sigma} = 0.0491]
Data/restraints/parameters	20957/6/1192
Goodness-of-fit on F^2	1.032
Final R indexes [I>=2σ (I)]	R_1 = 0.0436, wR_2 = 0.0972

Final R indexes [all data]	R_1 = 0.0610, wR_2 = 0.1125
Largest diff. peak/hole / e $Å^{-3}$	1.55/-1.15

3.5.10. Computational Details

Gaussian 16 software employing Density Functional Theory (DFT) calculations was utilized to optimize the structures of Ir(III) photocatalysts. Geometry optimization was executed utilizing the B3LYP functional with the LANL2DZ basis set.[13] Following unrestricted DFT calculations *in vacuo*, the optimized geometries were verified as true minima by the absence of imaginary vibrational frequencies. Subsequently, the geometries of the ground singlet state (S_1) and the first excited triplet state (T_1) were determined.

The CPCM implicit solvent model with water as a solvent was chosen to evaluate transition energies.[4] The ground state (S_0) geometry of the photocatalyst was obtained using restricted DFT. The first excited singlet state (S_1) geometry and first excited triplet state (T_1) geometry were obtained from unrestricted TD-DFT. The optimized S_0 and T_1 structures were confirmed to be local minima at the same computational level. FMOs were generated at the same level of theory.

3.5.11. Photocatalytic Reactions of 4-6 with NADH

The method for performing the photocatalytic reaction of photocatalyst **4/5/6 (**2 μM each**)** and NADH (240 μM) in DMSO:PBS (0.5:99.5, v/v) at different time intervals is provided in

Chapter II (**section 2.5.11**). The light used in this experiment was 525 nm (50.2 J cm^{-2}). TOF is calculated at 2 min.

3.5.12. Cyclic Voltammetry

Cyclic voltammetric measurements were done using a PAR model 273A electrochemistry system. A glassy carbon working electrode, a platinum wire auxiliary electrode, and a saturated calomel reference electrode (SCE) were used in a standard three-electrode configuration with tetrabutylammonium hexafluorophosphate as the supporting electrolyte (**5**, **6** concentration 1.0 mM; standard scan rate 100 mV s^{-1}). Cyclic voltammograms were scanned from −2.0 V to +2.0 V.

3.5.13. Detection of H_2O_2 Generation

In the reaction of photocatalyst **6** (2 μM) with NADH (240 μM) in DMSO:PBS (0.5:99.5, v/v) at ambient temperature in the dark or after light irradiation (525 nm, 50.2 J cm^{-2}), H_2O_2 was detected by Quantofix peroxide test sticks.

3.5.14. Determination of Singlet Oxygen Generation

The method for performing the singlet oxygen generation detection by photocatalysts **4/5/6** **(**2 μM each**)** in DMSO:PBS (0.5:99.5, v/v) is given in **Chapter II** (**section 2.5.13**). The light dose used was 525 nm (50.2 J cm^{-2}).

3.5.15. Determination of Hydroxyl Radical Generation

The production of photo-induced hydroxyl radicals by the photocatalysts was detected using the hydroxyl radical sensor methylene blue. Briefly, **4**/**5**/**6** (2 μM) in DMSO:PBS (0.5:99.5, v/v) was mixed with methylene blue (15 μM). The solution was then placed in quartz

cuvettes, followed by 525 nm (50.2 J cm^{-2}) light irradiation for different times at ambient temperature. The absorbance of the methylene blue was then monitored by UV-Vis. spectroscopy at ambient temperature.

3.5.16. MTT Assay

A cytotoxicity assessment was conducted on MCF-7, HeLa, and HEK-293 cells to evaluate the cytotoxic impact of photocatalysts **4/5/6** following the protocol given in **Chapter II (section 2.5.14)**. For hypoxic conditions (1% O_2), once the cells adhered, they were moved to a hypoxic incubator (1% O_2), where they were placed inside a biological safety cabinet within a glove box containing an atmosphere of 1% oxygen, 5% carbon dioxide, and 94% nitrogen for an additional 24 hours. This allowed the cells to adjust to low oxygen levels. Throughout the experiment, incubation occurred under consistent hypoxic conditions.

3.5.17. Sulforhodamine B (SRB) Assay

The cytotoxicity of the photocatalysts was evaluated *in vitro* using the SRB assay.[8] A549 cells were cultured in DMEM with 10% FBS and 1% penicillin-streptomycin solution at 37 °C under a 5% CO_2 atmosphere. Approximately 8000 cells were seeded into each well of a 96-well plate. The cells were then treated with various concentrations of the photocatalysts, starting at 50 µM and serially diluted down to 0.195 µM. The treatment was conducted in a medium composed of 1% DMSO and 99% DMEM for 4 h in the absence of light. After treatment, the medium was removed, and the cells were washed with DPBS. One group of cells was then exposed to visible light (400-700 nm) with an intensity of 10 J cm^{-2} for 1 h.

Following light exposure, the cells were replenished with fresh DMEM. The other group of cells was kept in the dark with fresh DMEM medium. Both sets of cells were incubated for an additional 43 h in the dark, completing a total incubation period of 48 h. For the SRB assay, 50 µL of cold 1% TCA was gently added to each well to achieve a final concentration of 10%. The plates were then incubated at 4 °C for 1 h to fix the cells. After fixation, the plates were washed four times with distilled water and allowed to air-dry. Subsequently, 100 µL of SRB dye solution (0.4% weight/volume in 1% acetic acid) was added to each well and incubated at room temperature for 1 h. The plates were then washed with 1% acetic acid to remove any unbound dye, air-dried again, and 100 µL of Tris buffer (10 mM, pH 10.5) was added to each well. The plates were gently shaken on a mechanical shaker for 15 min. Absorbance was measured at 564 nm using a microplate reader, and the IC_{50} values were calculated using GraphPad Prism 8 software.

3.5.18. Confocal Microscopy

In aseptic conditions, approximately 1×10^5 A549 cells were seeded onto glass-bottomed petri dishes and allowed to adhere for 24 h in a CO_2 incubator. Subsequently, a solution of the photocatalyst **6** at a concentration of 30 µM was introduced into the glass-bottom dishes, and the cells were incubated at 37 °C for 4 h. Following this incubation period, the cells were thoroughly washed with DPBS. To label specific organelles, the cells were then exposed to staining agents: Hoechst dye at a concentration of 5 µg/mL, and MitoTracker red at 250 nM. Finally, triple rinsing with PBS was performed, and images were acquired using an oil

immersion lens with a magnification of 63X. Image acquisition and processing were carried out utilizing ZEN 3.3 (blue edition software).

3.5.19. In-cell NADH Oxidation

The detection of NAD^+ and NADH in the cell lysate was done by the spectrophotometric assay described in the previous report.[43] Briefly, cells (1×10^6) were seeded into a 100 mm culture dish and allowed to adhere for 24 h. Following this, cells were treated with 25 μM of photocatalyst **6** and maintained under dark and light conditions as mentioned in the previous section. After light exposure, the cells were cultured for 24 h, harvested through trypsinization, and cell lysate prepared using Cellytic M® containing protease inhibitor cocktail. A portion of the cell lysate was used for the determination of protein content using the Bradford assay as per the manufacturer's instructions. The remainder of the cell lysate was divided into two aliquots and extracted in two different solutions: the alkali extraction for NADH and the acid extraction for NAD^+. Both extractions were adjusted to neutral pH before performing the recycling assay to determine the concentration of NAD^+ and NADH, as mentioned in the previous reference.

3.5.20. DCFH-DA Assay

The method to study the intracellular ROS by DCFH-DA assay in the presence of **6** (at a concentration of 1 μM) is given in **Chapter II (section 2.5.15)**. Incubation time with **6**: 4 h, Light irradiation (400-700 nm, 10 J cm^{-2}) for 1 h. Recovery after irradiation: 4 h. For the dark group, the light irradiation step was absent. The cells were treated with 10 μM DCFH-DA for staining. The flow cytometric examination was conducted utilizing FACS VERSE

equipment from BD Biosciences. The acquired data were subsequently processed and analyzed through FCS Express 7 software, developed by DeNovo Software.

3.5.21. JC-1 assay

The method to study the mitochondrial depolarization by JC-1 assay in the presence of **6** (at a concentration of 1 μM) is provided in **Chapter II (section 2.5.16)**. Incubation time with **6**: 4 h, Light irradiation (400-700 nm, 10 J cm^{-2}) for 1 h. Recovery after irradiation: 6 h. The images were captured at a 10X magnification. The acquired images were processed using ZEN 3.3 (blue edition) software.

3.5.22. Annexin V-FITC/Propidium Iodide Assay

This assay was performed following the protocol as described in **Chapter II (section 2.5.19)**. For this assay, photocatalyst **6** at a concentration of 2 μM was used. Incubation time with **6**: 4 h, Light irradiation (400-700 nm, 10 J cm^{-2}) for 1 h. Recovery after irradiation: 43 h. The cells were stained with 0.5 μL annexin and 0.5 μL propidium iodide and incubated for 10 minutes.

3.5.23. Caspase 3/7 Activity Assay

The method for caspase 3/7 activation study in the presence of **6** (at a concentration of 25 μM) is provided in **Chapter II (section 2.5.20)**. Incubation time with **6**: 4 h, Light irradiation (400-700 nm, 10 J cm^{-2}) for 1 h. Recovery after irradiation: 48 h.

3.5.24. Statistical Analysis

The outcome of the results was expressed as mean ± standard error of the three independent repeated experiments. Sample size, *i.e.*, n = 3, was used for respective statistical analysis. The statistical analysis was conducted utilizing SPSS 16.0 (SPSS, Chicago, IL, USA)

software. Results were compared between the dark control with the rest of the group (**6**, Control (Light), and **6**+Light). The statistical analysis was done by One-way ANOVA followed by Tukey's Post Hoc Test. Values of $p<0.05$ were considered statistically significant.

References

1. J. Karges, F. Heinemann, M. Jakubaszek, F. Maschietto, C. Subecz, M. Dotou, R. Vinck, O. Blacque, M. Tharaud, B. Goud, Z. N. E. Viñuelas, B. Spingler, I. Ciofini, G. Gasser, *J. Am. Chem. Soc*. **2020**, *142*, 6578-6587.
2. C. J. Hua, K. Zhang, M. Xin, T. Ying, J. R. Gao, J. H. Jiaa, Y. J. Li, *RSC Adv*. **2016**, *6*, 49221-49227.
3. C. Huang, C. Liang, T. Sadhukhan, S. Banerjee, Z. Fan, T. Li, Z. Zhu, P. Zhang, K. Raghavachari, H. Huang, *Angew. Chem. Int. Ed.* **2021**, *60*, 9474-9479Z.
4. Fan, J. Xie, T. Sadhukhan, C. Liang, C. Huang, W. Li, T. Li, P. Zhang, S. Banerjee , K. Raghavachari, H. Huang, *Chem. Eur. J*. **2022**, *28*, e202103346.
5. P. N. Lai, C. H. Brysacz, M. K. Alam, N. A. Ayoub, T. G. Gray, J. Bao, T. S. Teets, *J. Am. Chem. Soc*. **2018**, *140*, 10198-10207.
6. V. Novohradsky, A. Rovira, C. Hally, A. Galindo, G. Vigueras, A. Gandioso, M. Svitelova, R. Bresolí-Obach, H. Kostrhunova, L. Markova, J. Kasparkova, S. Nonell, J. Ruiz, V. Brabec, V. Marchán, *Angew. Chem. Int. Ed*. **2019**, *58*, 6311-6315.
7. S. S. Bhat, V. K. Revankar, R. V. Pinjari, S. Naveen, N. K. Lokanath, V. Kumbar, K. Bhate, D. G. Kokare, *New J. Chem*. **2018**, *42*, 16846-16854.

8. J. Kasparkova, A. H. García, H. Kostrhunova, M. Goicuría, V. Novohradsky, D. Bautista, L. Markova, M. D. Santana, V. Brabec, J. Ruiz, *J. Med. Chem*. **2024**, *11*, 691-708.
9. A. Shimizu, Y. Ishizaki, S. Horiuchi, T. Hirose, K. Matsuda, H. Sato, J. I. Yoshida, *J. Org. Chem*. **2021**, *86*, 770-781.
10. N. Kashyap, M. Rabha, S. K. Patra, B. Sen, S. K. Sheet, K. Baruah, S. Khatua, *Cryst. Growth Des*. **2024**, *24*, 3615-3631.
11. S. Ghosh, P. Paira, *Eur. J. Inorg. Chem.* **2025***, 28,* e202400769.
12. H. Huang, S. Banerjee, K. Qiu, P. Zhang, O. Blacque, T. Malcomson, M. J. Paterson, G. J. Clarkson, M. Staniforth, V. G. Stavros, G. Gasser, H. Chao, P. J. Sadler, *Nat. Chem*. **2019**, *11*, 1041-1048.
13. Gaussian 16, Revision A.03, M. J. Frisch, G. W. Trucks, H. B. Schlegel, G. E. Scuseria, M. A. Robb, J. R. Cheeseman, G. Scalmani, V. Barone, G. A. Petersson, H. Nakatsuji, X. Li, M. Caricato, A. V. Marenich, J. Bloino, B. G. Janesko, R. Gomperts, B. Mennucci, H. P. Hratchian, J. V. Ortiz, A. F. Izmaylov, J. L. Sonnenberg, D. Williams-Young, F. Ding, F. Lipparini, F. Egidi, J. Goings, B. Peng, A. Petrone, T. Henderson, D. Ranasinghe, V. G. Zakrzewski, J. Gao, N. Rega, G. Zheng, W. Liang, M. Hada, M. Ehara, K. Toyota, R. Fukuda, J. Hasegawa, M. Ishida, T. Nakajima, Y. Honda, O. Kitao, H. Nakai, T. Vreven, K. Throssell, J. A. Montgomery, Jr., J. E. Peralta, F. Ogliaro, M. J. Bearpark, J. J. Heyd, E. N. Brothers, K. N. Kudin, V. N. Staroverov, T. A. Keith, R. Kobayashi, J. Normand, K. Raghavachari, A. P. Rendell, J. C. Burant, S. S. Iyengar, J. Tomasi, M. Cossi, J. M. Millam, M. Klene, C. Adamo,

R. Cammi, J. W. Ochterski, R. L. Martin, K. Morokuma, O. Farkas, J. B. Foresman, and D. J. Fox, Gaussian 16, Inc., Wallingford CT, **2016**.

14. Z. Fan, Y. Rong, T. Sadhukhan, S. Liang, W. Li, Z. Yuan, Z. Zhu, S. Guo, S. Ji, J. Wang, R. Kushwaha, S. Banerjee, K. Raghavachri, H. Huang, *Angew. Chem. Int. Ed*. **2022**, *61*, e202202098.
15. X. Cui, J. Fan, Y. Gao, X. Zhou, C. Zhang, Q. Meng, *J. Med. Chem*. **2024**, *67*, 19826-19836.
16. L. Wei, R. Kushwaha, A. Dao, Z. Fan, S. Banerjee, H. Huang, *Chem. Commun*. **2023**, *59*, 3083-3086.
17. Z. Zhu, L. Wei, Y. Lai, W. L. O. Carter, S. Banerjee, P. J. Sadler, H. Huang, *Dalton Trans*. **2022**, *51*, 10875-10879.
18. U. Das, P. Paira, *Dalton Trans*. **2024**, *53*, 6459-6471.
19. L. Qiao, J. Liu, S. Kuang, X. Liao, J. Kou, L. Ji, H. Chao, *Dalton Trans*. **2021**, *50*, 14332-14341.
20. A. Bera, S. Gautam, S. Sahoo, A. K. Pal, P. Kondaiah, A. R. Chakravarty, *RSC. Med. Chem*. **2022**, *13*, 1526-1539.
21. A. A. Mandal, V. Singh, S. Saha, S. Peters, T. Sadhukhan, R. Kushwaha, A. K. Yadav, A. Mandal, A. Upadhyay, A. Bera, A. Dutta, B. Koch, S. Banerjee, *Inorg. Chem*. **2024**, *63*, 7493-7503.
22. R. T. Ryan, K. C. Stevens, R. Calabro, S. Parkin, J. Mahmoud, D. Y. Kim, D. K. Heidary, E. C. Glazer, J. P. Selegue, *Inorg. Chem*. **2020**, *59*, 8882-8892.

23. S. Liu, J. Han, W. Wang, Y. Chang, R. Wang, Z. Wang, G. Li, D. Zhu, M. R. Bryce, *Dalton Trans*. **2022**, *51*, 16119-16125.

24. J. Karges, S. Kuang, F. Maschietto, O. Blacque, I. Ciofini, H. Chao, G. Gasser, *Nat. Commun.* **2020**, *11*, 3262.

25. J. V. Meerloo, G. J. Kaspers, J. Cloos, *Methods Mol. Biol*. **2011**, *731*, 237-245.

26. N. P. Bigham, J. J. Wilson, *Eur. J. Inorg. Chem*. **2023**, *26*, e202200735.

27. G. Sahu, S. A. Patra, S. Lima, S. Das, H. Görls, W. Plass, R. Dinda, *Chem. Eur. J.* **2023**, *29*, e202202694.

28. S. Kuang, F. Wei, J. Karges, L. Ke, K. Xiong, X. Liao, G. Gasser, L. Ji, H. Chao, *J. Am. Chem. Soc*. **2022**, *144*, 4091-4101.

29. V. Singh, N. K Rana, M. Kashif, P. P. Manna, T. S. B. Baul, B. Koch, *Toxicol In Vitro,* **2023**, *86*, 105484.

30. S. Nikolić, J. Arakelyan, V. Kushnarev, S. M. Alfadul, D. Stanković, Y. I. Kraynik, S. G. Šipka, M. V. Babak, *Inorg. Chem*. **2023**, *62*, 8188-8199.

31. A. C. Carrasco, V. R. Fanjul, A. Habtemariam, A. M. Pizarro, *J. Med. Chem*. **2020**, *63*, 4005-4021.

32. D. G. Nicholls, M. W. Ward, *Trends Neurosci*. **2000**, *23*, 166-174.

33. M. Reers, T. W. Smith, L. B. Chen, *Biochemistry* **1991**, *18*, 4480-4486.

34. A. Upadhyay, A. Nepalia, A. Bera, D. K. Saini, and A. R. Chakravarty, Platinum (II) boron-dipyrromethene complex for cellular imaging and mitochondria-targeted photodynamic therapy in red light. *Chem. Asian J.,* **2023**, *18*, e202300667.

35. P. Goswami, V. Singh, B. Koch, *J. Ethnopharmacol*. **2024**, *334*, 118537.

36. H. R. Stennicke, J. M. Jurgensmeier, H. Shin, Q. Deveraux, B. B. Wolf, X. Yang, Q. Zhou, H. M. Ellerby, L. M. Ellerby, D. Bredesen, *J. Biol. Chem*. **1998**, *273*, 27084-27090.

37. Z. Molphy, A. Prisecaru, C. Slator, N. Barron, M. McCann, J. Colleran, D. Chandran, N. Gathergood, A. Kellett, *Inorg. Chem*. **2014**, *53*, 5392-5404.

38. M. Mariappan, B. G. Maiya, *Eur. J. Inorg. Chem*. **2005**, *2005*, 2164-2173.

39. G. M. Sheldrick, SADABS, a software for empirical absorption correction, Ver. 2.05, University of Göttingen, Göttingen, Germany, **2002**.

40. G. M. Sheldrick, *Acta Cryst.* **2015**, *71*, 3-8.

41. O. V. Dolomanov, L. J. Bourhis, R. J. Gildea, J. A. K. Howard, H. A. Puschmann, *J. Appl. Cryst*. **2009**, *42*, 339-341.

42. G. M. Sheldrick, *Acta Cryst*. **2008**, *64*, 112-122.

43. C. T. Zhu, D. M. Rand, *PLoS One*. **2012**, *7*, e47584.